

# Revisiting $^7\text{Be}$ Weak and Radiative Transition Rates in Big Bang Nucleosynthesis: Implications for the Primordial Lithium Problem

Simone Taioli<sup>1, 2, 3\*</sup>, Francesca Triggiani<sup>4</sup>, and Stefano Simonucci<sup>5, 6\*</sup>

<sup>1</sup> European Centre for Theoretical Studies in Nuclear Physics and Related Areas (ECT\*), Bruno Kessler Foundation, Strada delle Tabarelle, 286, 38123 Trento, Italy

<sup>2</sup> Trento Institute for Fundamental Physics and Applications (TIFPA-INFN), Via Sommarive, 14, 38123 Trento, Italy

<sup>3</sup> INAF, Observatory of Abruzzo, Via Mentore Maggini snc, 64100 Teramo, Italy

<sup>4</sup> National Institute for Nuclear Physics (INFN), Sezione di Milano, Via Celoria 16, 20133 Milano, Italy.

<sup>5</sup> School of Science and Technology – Physics Division, University of Camerino, Via Madonna delle Carceri, 9B, 62032 Camerino, Italy

<sup>6</sup> National Institute for Nuclear Physics (INFN), Sezione di Perugia, Via Alessandro Pascoli, 23c, 06123 Perugia, Italy

e-mail: stefano.simonucci@unicam.it  
e-mail: taioli@ectstar.eu

January 21, 2026

## ABSTRACT

**Context.** The primordial  $^7\text{Li}$  abundance predicted by standard Big Bang Nucleosynthesis (BBN) exceeds the value inferred from old, metal-poor stars by a factor of approximately 3–4. In this model, most primordial  $^7\text{Li}$  is produced as  $^7\text{Be}$  in the early Universe and subsequently converted by electron capture (EC). However, any additional production or destruction channels for  $^7\text{Be}$ , such as proton capture (PC) or antineutrino capture (AC) during BBN, may affect the final  $^7\text{Li}$  yield.

**Aims.** We quantify the effect on  $^7\text{Be}$  depletion of (i) in-situ EC, including the corresponding AC channel, during the Big Bang epoch; (ii) positron decay from the Be nuclear excited state; and (iii) PC via both the standard radiative channel  $^7\text{Be}(p, \gamma)^8\text{B}$ , including the possibility of stimulated emission (SE) due to the dense  $\gamma$  photon background present during the nuclear statistical equilibrium (NSE) epoch, as well as by analysing the possible contribution of a three-body “Auger-like” variant in which the capture energy is transferred to a continuum electron.

**Methods.** Decay rates are calculated using first-order perturbation theory, modelling weak decay with a Fermi contact interaction and factorising hadronic and leptonic currents in the transition operator matrix element. The field operators describing hadrons and leptons are determined using mean-field methods. Thermally averaged nuclear rates were obtained by folding the relevant cross-sections with Maxwell–Boltzmann distributions and accounting for the number density of the particle triggering the nuclear reaction in the temperature range  $10 \text{ keV} < k_{\text{B}}T < 100 \text{ keV}$ , below the NSE epoch. For  $^7\text{Be}(p, \gamma)^8\text{B}$ , we used the astrophysical  $S_{17}$  factor and included Debye screening. The SE channel is addressed using the quantum field theory formalism. The Auger-like cross-section was derived using a plane-wave electron approximation and evaluated numerically at representative BBN temperatures and densities.

**Results.** The calculated  $^7\text{Be}$  EC rate decreases rapidly over time (as temperature decreases) and is significantly enhanced when the antineutrino channel is included. The thermally averaged  $^7\text{Be}(p, \gamma)^8\text{B}$  rate increases only slightly when the nuclear SE mechanism and plasma screening are considered (1–3% at  $k_{\text{B}}T \simeq 87 \text{ keV}$ ). The Auger-like three-body capture has a cross-section approximately a few thousandths of a percent of that of the radiative channel at all temperatures, but becomes negligible (about  $10^{-10}$  of the radiative channel) by  $k_{\text{B}}T \simeq 10 \text{ keV}$ . Our total rate revises previous estimates based on systematics by nearly a factor of ten.

**Conclusions.** Within the approximations adopted here,  $^7\text{Be}$  EC, PC, and  $\beta^+$  decay provide percent-level corrections to the fastest and dominant depletion channel,  $^7\text{Be}(n, p)^7\text{Li}$ , which is followed by the rapid destruction  $^7\text{Li}(p, \alpha)^4\text{He}$ . Although these decays are unlikely on their own to resolve the cosmological lithium discrepancy with observations, the use of first-principles simulations, leading to a correction of about one order of magnitude for the half-life (approximately one day), helps to close the gap with observations of old halo stars. Our first-principles study paves the way for a complete reassessment of the network of all nuclear transitions to quantify accurately the abundance of  $^7\text{Li}$  within established nuclear and atomic physics models, but beyond semi-empirical approximations based on  $\log(f)$  systematics, and before considering interpretations that assume physics beyond the Standard Model (BSM).

**Key words.** Big Bang Nucleosynthesis, early Universe, electroweak decays, strong interaction, isotopic abundances of light nuclei, the cosmological lithium problem

## 1. Introduction

Lithium holds a unique position in nuclear astrophysics, as it is one of the few elements synthesised during the Big Bang. However, the enrichment of lithium in the Universe remains an open problem, presenting several unresolved challenges to stellar and Galactic chemical evolution models, as well as to Big Bang Nucleosynthesis (BBN) (Bertulani et al. 2018;

Miranda, Oswaldo D. 2025).

In this context, observational evidence from the Sun and solar analogues indicates significant lithium depletion, with photospheric abundance approximately two orders of magnitude lower than meteoritic values (Asplund et al. 2009). In stars less massive than the Sun, where the convective envelope remains extended even during the main sequence (MS), lithium destruction continues throughout this phase. Pronounced lithium

depletion is also observed in other MS stars, specifically F-type stars with masses between 1.2 and 1.5  $M_{\odot}$ , at intermediate temperatures (6400–6900 K) in the Galactic disc. These stars undergo the so-called Li dip, attributed to non-standard mixing processes such as rotationally induced transport and microscopic diffusion (Boesgaard & Tripicco 1986a,b; Balachandran 1995). In contrast, in higher-mass stars, the outer convective regions are expected to contract and no longer reach layers hot enough to deplete lithium.

A particularly important issue is determining reliable electron capture (EC) and proton capture (PC) rates on  $^7\text{Be}$ , which significantly affect  $^7\text{Li}$  abundance, under temperature and density conditions that may differ from those on Earth and can vary by orders of magnitude between the envelope and the stellar interior. In stellar plasma, significant uncertainties remain in the temperature and density dependence of nuclear reaction rates, particularly due to possible electron degeneracy. In the solar core, for example, the temperature is slightly too high and the density too low for electron degeneracy, so electrons can be treated as a classical gas. However, a decreasing radius upon gravitational collapse can lead to degeneracy. In such cases, the widely used Debye-Hückel (DH) approximation for modelling electron screening (Bahcall 1962; Bahcall & Moeller 2018) can be questionable, as the de Broglie wavelength becomes comparable to the interparticle distance in the astrophysical plasma.

In this context, a new temperature- and density-dependent rate for the electron capture (EC) of Be in evolved stars undergoing the red giant branch (RGB) and asymptotic giant branch (AGB) phases was proposed (Simonucci et al. 2013; Palmerini et al. 2016), using a mean-field ab initio approach based on the numerical solution of the quantum mechanical equation of motion. Higher electron densities at the nucleus, calculated by a Hartree-Fock (HF) approach, result in more effective EC and a revision of the  $^7\text{Be}$  lifetime, which is shorter than that predicted by the DH model used by Bahcall (Bahcall 1962; Bahcall & Moeller 2018), on which the solar-extrapolated rates from Adelberger (Adelberger et al. 2011) are based. The new rate, applied to low-mass (2–3  $M_{\odot}$ ) stars of solar metallicity under the influence of deep-mixing processes, established lower equilibrium abundances of  $^7\text{Be}$  in the layers above the H-burning shell of AGB stars.

Furthermore, a shorter lifetime for  $^7\text{Be}$  EC results in a maximum difference of about 4% in the efficiency of the  $^7\text{Be}$  channel (Vescovi et al. 2019) compared to previous estimates (Iben Jr et al. 1967). This, in turn, affects the relative importance of the PC channel on Be via the  $^7\text{Be}(p,\gamma)^8\text{B}$  process, which is crucial for interpreting terrestrial measurements of the solar neutrino flux from  $^8\text{B}$ .

We note that electroweak decay rates are also expected to depend sensitively on the ionisation state and local level population distributions of the plasma, resulting in non-local thermodynamic equilibrium (NLTE) conditions that can alter both the electron density at the nucleus and the effective screening potential (Mascali et al. 2022, 2023; Agodi et al. 2023). For example, the effect of considering NLTE has been assessed in low-density laboratory magnetoplasmas and compared with high-density collision-driven local thermodynamic equilibrium (LTE) plasmas, revealing a significant impact (Mishra et al. 2024). Therefore, a precise evaluation of these effects is desirable for modelling lithium production and destruction pathways in astrophysical sites, and to achieve a consistent picture of Galactic  $^7\text{Li}$  nucleosynthesis. While our treatment is limited to LTE, we accurately include ionisation and excitation in our

model.

Apart from the unsatisfactory determination of  $^7\text{Li}$  in MS and evolved stars, its primordial abundance in the early Universe also shows considerable uncertainty and problematic estimation. In fact, while the abundances of light nuclei such as  $^1\text{H}$ ,  $^2\text{H}$ ,  $^3\text{He}$ , and  $^4\text{He}$ , also synthesised during the Big Bang, are in excellent agreement with predictions from BBN models when the baryon density inferred from the Cosmic Microwave Background (CMB) is used,  $^7\text{Li}$  does not fit and is the only significant (exceeding  $5\sigma$ ) outlier (Cyburt et al. 2016; Pitrou et al. 2018). The primordial abundance of  $^7\text{Li}$  is inferred from spectroscopic observations of old, metal-poor Population II halo stars of sub-solar mass, whose long lifespans preserve their original chemical composition, as they formed soon after the Big Bang from gas that had not yet been significantly enriched by later generations of stars.  $^7\text{Li}$  nearly constant value in the atmospheres of low-metallicity halo stars observed across a range of effective temperatures – the Spite plateau (Spite & Spite 2012) – and the detection of the more fragile  $^6\text{Li}$  isotope of cosmic-ray origin support the idea that these stars retain the early Universe signature without significant stellar depletion (Bonifacio et al. 2007).

In particular, observations from the Wilkinson Microwave Anisotropy Probe (WMAP) and Planck collaborations show that the primordial abundance of  $^7\text{Li}$  – referring to lithium synthesised during the early phases of our Universe, not in stars – is lower than standard BBN predictions by a factor of 3–4 (i.e.  $(^7\text{Li}/\text{H})_{\text{BBN}} \simeq (4\text{--}5) \times 10^{-10}$  vs.  $(^7\text{Li}/\text{H})_{\text{obs}} \simeq (1.3\text{--}1.6) \times 10^{-10}$ ) (Coc & Vangioni 2017; Sivarani et al. 2004). By contrast, in the interstellar medium,  $^7\text{Li}$  abundance is higher than expected from BBN (Casuso & Beckman 2003).

Several possible explanations have been proposed, including: i) astrophysical depletion of surface  $^7\text{Li}$  through cosmic rays, rotational mixing (Michaud 1986; Charbonnel & Lagarde 2010; Andrews et al. 1988), magnetic dynamo processes (Eggenberger et al. 2010), or diffusion and transport processes (Michaud & Charbonneau 1991) after star formation during the early stages (and MS). These processes may lead to lithium destruction when convective motions carry it to temperatures of a few million K, where it undergoes PC; ii) systematic uncertainties arising from NLTE and three-dimensional effects in stellar plasmas, which may result in a lower estimate of lithium abundances due to much higher rates compared to LTE (Mishra et al. 2024); iii) nuclear physics uncertainties in reaction rates, such as  $^3\text{He}(\alpha,\gamma)^7\text{Be}$ , or weak decays, including excited nuclear and electronic states, which could, in principle, modify the predicted yield; and iv) physics beyond the Standard Model (BSM), which can lead to modified nuclear reaction rates during BBN that may differ slightly from those assumed, variations in fundamental constants, or inhomogeneous baryon distributions, which could have altered the primordial lithium yield without affecting the agreement found for deuterium abundance.

Thus, despite extensive theoretical (Simonucci et al. 2013; Palmerini et al. 2016; Vescovi et al. 2019), experimental (Damone et al. 2018) and observational (Fields 2011; Richard et al. 2005; Fields & Olive 2022) efforts, no universally accepted solution has been found to this long-standing discrepancy between BBN theoretical predictions and astrophysical measurements. This discrepancy persists even with updated experimental nuclear reaction rates, whose accuracy should make large deviations unlikely, and with revised cosmological parameters. This issue is known as the *cosmological lithium problem* and remains one of the few unresolved tensions within

the otherwise successful framework of standard BBN.

The aim of this work is to revisit some weak and strong nuclear reaction rates as well as to investigate previously unconsidered processes that may have influenced the  ${}^7\text{Li}$  abundance synthesised under the conditions of the earliest stages of the Universe using ab initio simulations. It is plausible that certain nuclear reactions have either not been properly considered or have been treated with methods that yielded unsatisfactory accuracy in the temperature and density dependence of the rates. In this context, using first-principles approaches in relativistic atomic and nuclear physics could bring theoretical predictions into closer agreement with the data. Implicit in our approach is the assumption that conventional atomic and nuclear physics, which broadly support the standard BBN model, can account for the primordial lithium problem before attributing the remaining discrepancy concerning the lithium isotope to unknown nuclear physics. In particular, within our ab initio framework (Morresi et al. 2018; Taioli & Simonucci 2021; Taioli et al. 2022), we examine weak interaction decays that may have affected  ${}^7\text{Li}$  abundance, specifically those that convert  ${}^7\text{Be}$  into  ${}^7\text{Li}$ , such as EC, antineutrino capture (AC), and positron emission from nuclear states excited under conditions present during the Big Bang. Moreover, we compute the PC decay of Be during BBN, considering the possibility that (i) the capture energy released via  $\gamma$  photons is transferred to a continuum electron, analogous to the Auger effect; and (ii) the presence of a dense  $\gamma$  photon background can induce nuclear stimulated emission (SE).

Earlier studies (Fuller et al. 1982; Fuller & Smith 2010) concluded that some of these channels were negligible, using  $\log(f/t)$  values determined in laboratory settings from systematics (National Nuclear Data Center 2023) and extrapolated to early Universe conditions. In particular, the half-life of some of the transitions considered here, as found with these extrapolations, was too long (approximately 10 days (Fuller & Smith 2010)) for these nuclei to have been synthesised during the first thousands of seconds after the Big Bang, when conditions for nuclear formation were optimal. However, nucleosynthesis of light elements after the Big Bang occurred in a hot, dense, highly ionised, relativistic plasma, where rates can differ significantly. The first experimental indications that  $\beta$  decays can be influenced by a high degree of atomic ionisation were obtained in storage rings (Litvinov & Bosch 2010), which enabled measurements of  $\beta$  decay rates in fully stripped atoms. One of the most striking results was that completely ionised  ${}^{187}\text{Re}^{75+}$  ions decay nine orders of magnitude faster than neutral  ${}^{187}\text{Re}$ , which has a half-life of 42 Gyr. This dramatic difference is due to a decay channel known as bound-state  $\beta$  decay – typically forbidden in neutral atoms – in which the emitted electron is captured into one of the atom's inner shells. In addition, nuclear excitations of both parent and daughter isotopes, possible at the temperatures in the early phases of our Universe, can also dramatically modify the rates. To investigate plasma-induced modifications of  $\beta$  decay rates, such as those predicted by the Takahashi and Yokoi (TY83) model (Takahashi & Yokoi 1983, 1987), the PANDORA facility (Plasmas for Astrophysics, Nuclear Decay Observations and Radiation for Archaeometry) is being developed at INFN–LNS (Catania, Italy) (Mascali et al. 2022). It is based on an electron cyclotron resonance (ECR) magnetoplasma designed to enable in-plasma measurements of  $\beta$  decay rates.

Therefore, we recalculate these decay rates using first-principles simulations, incorporating finite temperature (i.e., atomic and nuclear excitation and ionisation) and density effects,

to provide input better matched to cosmological conditions and enable a new assessment of their impact on the  ${}^7\text{Li}$  abundance, which remains too high compared with observations.

## 2. Reassessment of the cosmological ${}^7\text{Li}$ problem

The early thermal history of our Universe, relevant to baryon evolution and primordial nucleosynthesis, can be described as a sequence of freeze-outs, because the nuclear reaction rates  $\Gamma$  decrease as the Universe expands and cools. In particular, detailed balance among reactants and products of nuclear reactions leading to nucleosynthesis is maintained only while

$$\Gamma > \frac{1}{t}, \quad (1)$$

where  $t$  is the cosmic age, defined as the time elapsed since the singularity at the beginning of the Universe. According to BBN, for example, in a reaction such as  $\gamma + \gamma \leftrightarrow e^- + e^+$ , where lepton-antilepton pairs  $e^\pm$  are produced by and in equilibrium with  $\gamma$  photons, the interaction rate is given by  $\Gamma = \langle n_\gamma v_{\text{rel}} \sigma \rangle$ , where  $n_\gamma$  is the  $\gamma$  photon density,  $v_{\text{rel}}$  is the relative velocity, and  $\sigma$  is the interaction cross-section. When condition (1) is no longer satisfied, the expansion of the Universe outpaces the reaction rate, pair creation can no longer balance annihilation, so the species decouple and their abundance relative to photons becomes fixed (freeze-out).

The cosmic age in Eq. (1) is related to the photon temperature by  $T \equiv T_\gamma \propto t^{-1/2}$  (Perkins 2009), where  $T_\gamma$  is the  $\gamma$  photon temperature. This temperature can also serve as a timescale to indicate the various epochs of the early Universe. At  $k_B T \gtrsim 200$  MeV, the plasma is a quark–gluon fluid. Between  $k_B T \simeq 200$  and 20 MeV, baryons (antibaryons)  $b$  ( $\bar{b}$ ) remain in equilibrium with photons via  $\gamma + \gamma \leftrightarrow b + \bar{b}$ , while below  $k_B T \lesssim 100$  MeV, only light nucleons (antineucleons), such as protons  $p$  (antiprotons  $\bar{p}$ ) and neutrons  $n$  (antineutrons  $\bar{n}$ ), survive. Their pair production freezes out at  $k_B T \approx 20$  MeV, while transient deuterium formation is promptly erased by photodisintegration. In this context, we note that the WMAP baryon asymmetry,  $(n_b - n_{\bar{b}})/n_\gamma = 6.11 \times 10^{-10}$ , reflects the primordial matter–antimatter imbalance.

Electrons, positrons, and neutrinos remain coupled to radiation through  $\gamma + \gamma \leftrightarrow e^- + e^+ \leftrightarrow \nu + \bar{\nu}$  until neutrino decoupling at  $k_B T \approx 3$  MeV and  $e^\pm$  decoupling at  $k_B T \approx 1$  MeV. Weak interactions maintain  $n/p$  equilibrium down to  $k_B T \approx 700$  keV (weak freeze-out), after which only  $\beta^-$  decays can change the  $n/p$  ratio until  $k_B T \approx 100$  keV, when neutrons become bound in  $\alpha$  particles and the  $n/p$  ratio freezes (the so-called Nuclear Statistical Equilibrium, NSE). The breakdown of  $n + p \leftrightarrow {}^2\text{H} + \gamma$  at  $k_B T \approx 50$ –60 keV allows deuterium to survive and enables the synthesis of light nuclei, such as  ${}^7\text{Li}$  and  ${}^7\text{Be}$ .

In this work, we calculate the reaction rates of the channels contributing to the formation and depletion of  ${}^7\text{Li}$  during the Big Bang, in the temperature range 100 to 10 keV, below NSE when conditions allowed these nuclei to form. All these reactions proceed through  ${}^7\text{Be}$  as the intermediate nucleus (Fuller & Smith 2010; Fields et al. 2014). In the BBN model,  ${}^7\text{Be}$  is produced primarily by  ${}^3\text{He}(\alpha, \gamma){}^7\text{Be}$ ,<sup>1</sup> at temperatures of 50–60 keV, while the dominant production channel of primordial lithium is the  ${}^7\text{Be}(n, p){}^7\text{Li}$  reaction ( $Q$ -value = 1.64 MeV), characterised by a large cross-section owing to the still high free neutron density, followed by  ${}^7\text{Li}(p, \alpha){}^4\text{He}$ . However, by the time BBN reaches

<sup>1</sup> Note that the reaction  ${}^6\text{Li}(p, \gamma){}^7\text{Be}$  makes a much smaller contribution due to the very low primordial  ${}^6\text{Li}$  abundance.

the stage where  ${}^7\text{Be}$  is abundant ( $t \approx 300$  s, corresponding to temperatures well below NSE), free neutrons have dropped significantly, having been trapped in bound states, mostly as  $\alpha$  particles. Consequently, the slower pace of the  ${}^7\text{Be}(n, p){}^7\text{Li}$  reaction is no longer sufficient to destroy all Be. Moreover, photodisintegration of  ${}^7\text{Be}$  is negligible because photons with  $E_\gamma \geq 1.586$  MeV (for  ${}^7\text{Be} + \gamma \rightarrow {}^3\text{He} + {}^4\text{He}$ ) or  $E_\gamma \geq 5.60$  MeV (for  ${}^7\text{Be} + \gamma \rightarrow {}^6\text{Li} + p$ ) are exponentially rare at BBN temperatures  $\lesssim 0.1$  MeV. As a result, most  ${}^7\text{Be}$  survives and decays to  ${}^7\text{Li}$  through various electroweak processes producing the cosmological excess in BBN compared to that observed in low-metallicity halo stars.

In this context, our analysis examines three electroweak processes responsible for the production of  ${}^7\text{Li}$  under NSE conditions. Specifically, we performed the ab initio calculation of the EC process,



and, as it is driven by the same interaction Hamiltonian, the AC,



and



where  ${}^7\text{Be}^*$  denotes the first excited nuclear state of Be. We emphasise that although neutrino interactions are typically elusive, we assess whether the high densities of electron antineutrinos in the early Universe could make this channel relevant for  ${}^7\text{Be}$  destruction (or  ${}^7\text{Li}$  production). As the Universe expands and cools, the antineutrino background becomes diluted, causing the contribution from this channel to become rapidly negligible.

Among the possible reactions leading to  ${}^7\text{Be}$  destruction (and thus to a lower production of  ${}^7\text{Li}$ ), there is also the strong force-driven PC, for which we compute the rate here under Big Bang conditions below NSE ( $10 \text{ keV} < k_B T < 100 \text{ keV}$ ) to determine its impact on primordial abundance and assess whether this can reconcile the cosmological lithium problem. Specifically, we study the following mechanism:



which is a non-resonant radiative PC process driven by both the strong and electromagnetic interactions, and dominated by direct E1 transitions. In this regard, we first use classical non-relativistic methods, supplemented by experimentally determined cross-sections. Second, more accurate quantum mechanical calculations are performed to account for the likely presence of a highly energetic photon background, which may alter the rate through a mechanism similar to SE in lasers between nuclear levels. Moreover, we consider a three-body variant of the process (5) in which the PC energy gain is transferred to a free electron in the surrounding plasma via a virtual photon (an Auger-like process in the continuum), as follows:



This energy transfer mechanism, typically neglected in astrophysical scenarios, can modify PC under NSE conditions, analogous to internal conversion in atomic systems.

Finally, the resulting new weak and radiative interaction rates for these processes, including temperature, density and charge state effects are essential inputs for recalculating nuclide abundances within the BBN model.

### 3. Electron and antineutrino capture on ${}^7\text{Be}$ : theoretical and computational methods

Our initial calculations address the EC (see Eq. (2)), AC (see Eq. (3)), and excited-state positron emission (see Eq. (4)) on  ${}^7\text{Be}$  under thermal conditions in which Be begins to form ( $10 \text{ keV} < k_B T < 100 \text{ keV}$ ).

Typically, the EC rate for a given transition between nuclear levels of parent and daughter nuclei is determined by obtaining the nuclear transition matrix element from the  $\log(ft)$  value, where  $f$  is the lepton phase volume describing the phase space accessible to the electron and neutrino during the decay, and  $t \equiv t_{1/2}$  is the half-life (Bahcall 1961).  $\log(ft)$ s are typically estimated by analogy to laboratory decays of nearby nuclei with similar transitions, which can result in a large range of values, the so-called systematics. Finally, the transition rate can be obtained by including the shape factor  $S$ , which accounts for forbiddenness, and the Fermi function  $F(Z, w)$ , where  $Z$  is the atomic number of the decaying nucleus and  $w$  is the ratio of the electron momentum to its energy (Fuller & Smith 2010). The Fermi function accounts for Coulomb distortion of the incoming electron or escaping positron wave functions. In this context, the Coulomb repulsion between electrons in the plasma and the electron-nuclear attraction are treated using an average Coulomb wave correction factor, which is also included in the Fermi function. Earlier works (Fuller & Smith 2010), based on systematics, assumed LTE and that weak interaction rates depend polynomially on plasma (electron) temperature, with a Fermi-Dirac occupation of the orbitals for both electron and neutrino fermionic species. While this standard approach may work well for predicting the lineshape of allowed and forbidden unique transitions, it fails, for example, for forbidden non-unique transitions, where there is no simple relation for  $S$  and the systematics provide too broad a range of values, reflecting uncertainty about the nuclear levels involved. This approach was used to estimate isotope half-life in highly ionised plasma in the seminal work by Takahashi and Yokoi (Takahashi & Yokoi 1987; Takahashi et al. 1987), which, after 35 years, remains the most widely used method for calculating primordial and stellar nucleosynthesis, despite the semi-empirical treatment of the hadronic and leptonic currents.

On the contrary, we do not rely on semi-empirical approaches based on the determination of  $\log(ft)$  values and  $F(Z, w)$ ; instead, we have developed a theoretical and computational framework (Taioli & Simonucci 2021; Taioli et al. 2022), using first-principles simulations to calculate the EC rates by determining the local electron density at the nucleus, to which the rate is proportional, modulo some weighting factors. This method fully incorporates relativistic (and quantum electrodynamical) effects. Within this framework, we can account for several factors influencing the EC, such as electron-electron interaction, charge state distribution, and electron and nuclear excitation of the parent and daughter atoms at the same level of theory. A significant difference in our approach concerns the treatment of the leptonic current, which is typically included using a semi-empirical Fermi function. In contrast, we use first-principles simulations based on the Dirac-Hartree-Fock (DHF) method to determine the electronic wave functions that enter the leptonic current, accounting for the population-level distribution and charge state of the parent Be ion undergoing beta decay and the Li daughter nucleus. This includes non-orthogonality between initial and final states, shake-up, shake-off, the energy continuum and the integration of the electronic degrees of freedom within the nuclear range. Temperature enters into the assessment of the chemical potential of the species and influences

the local density of bound and continuum electrons at the Be nucleus. In this respect, we have demonstrated (Taioli et al. 2022) the importance of accurately including the leptonic part, which may decrease, for example, the half-life of beta-decaying  $^{134}\text{Cs}$  isotopes by 20% in the range [0, 15] keV compared to the frozen-electron-only beta decay rate. In contrast, the rate may increase by a factor of 15 between 10 and 100 keV compared to room temperature conditions, where  $\log(f_t)$  values are measured, due to the inclusion of fast-decaying nuclear excited states.

Moreover, we assess the nuclear transition matrix elements that enter the hadronic currents using a mean-field approach, similar to the independent-particle nuclear shell model, by solving the Dirac equation for the nucleons with a relativistic Woods-Saxon nuclear potential. This mean-field approach can, of course, be systematically improved by employing more correlated many-body techniques without altering the foundation of our method.

The EC rate on  $^7\text{Be}$  was calculated to first order in time-dependent perturbation theory, using Fermi's golden rule in atomic units (Morresi et al. 2018),

$$\Gamma_{i \rightarrow f} = 2\pi |\langle f | \hat{V} | i \rangle|^2 \rho_i \rho_f \delta(E_i - E_f), \quad (7)$$

where  $\hat{V}$  is the weak interaction Hamiltonian,  $\rho_i$  and  $\rho_f$  are the initial and final densities of states, and the delta function enforces energy conservation between the initial and final state energies  $E_i$  and  $E_f$ , respectively. The weak interaction is described within the Fermi theory of beta decay by the effective potential

$$\hat{V} = \frac{G_F}{\sqrt{2}} \int d^3r \left[ \hat{\psi}_p(\mathbf{r}) \gamma^\mu (1 - x\gamma^5) \hat{\psi}_n(\mathbf{r}) \right. \times \\ \left. \left[ \hat{\psi}_e(\mathbf{r}) \gamma_\mu (1 - \gamma^5) \hat{\psi}_\nu(\mathbf{r}) \right] + \text{h.c.}, \right] \quad (8)$$

where  $G_F = 1.16637 \times 10^{-5}$  GeV $^{-2}$  is the Fermi coupling constant, and  $x = C_A/C_V = 1.26 \pm 0.02$  is the ratio of the axial vector ( $C_A$ ) to vector ( $C_V$ ) contributions to the hadronic current, and  $\gamma^\mu$  ( $\mu = 1, \dots, 5$ ) are the Dirac matrices. In Eq. (8),  $\hat{\psi}_p(\mathbf{r})$ ,  $\hat{\psi}_n(\mathbf{r})$ ,  $\hat{\psi}_e(\mathbf{r})$ , and  $\hat{\psi}_\nu(\mathbf{r})$  are the field operators for the proton, neutron, electron, and neutrino, respectively. For each field operator  $\hat{\psi}$ , the corresponding conjugate  $\bar{\psi} = \psi^\dagger \gamma^0$  is defined using the following Dirac matrix:

$$\gamma^0 = \begin{pmatrix} I & 0 \\ 0 & -I \end{pmatrix}, \quad (9)$$

where  $I$  and  $0$  are the  $2 \times 2$  identity and zero matrices, respectively.

The matrix element of the interaction potential in Eq. (8) between the initial (parent nucleus, labelled  $i$ ) and final (daughter nucleus, labelled  $f$ ) states factorises into purely hadronic ( $p, n$  label proton and neutron) and leptonic ( $e, \nu$  label electron and neutrino) currents as follows (Morresi et al. 2018; Taioli & Simonucci 2021):

$$\langle f | \hat{V} | i \rangle = \frac{G_F}{\sqrt{2}} \int d^3r \left[ \langle f_{p,n} | \hat{\psi}_p(\mathbf{r}) \gamma^\mu (1 - x\gamma^5) \hat{\psi}_n(\mathbf{r}) | i_{p,n} \rangle \right. \times \\ \left. \left[ \langle f_{e,\nu} | \hat{\psi}_e(\mathbf{r}) \gamma_\mu (1 - \gamma^5) \hat{\psi}_\nu(\mathbf{r}) | i_{e,\nu} \rangle \right] + \text{c.c.} \right] \\ = \frac{G_F}{\sqrt{2}} \int d^3r \left[ \langle f_p | \hat{\psi}_p(\mathbf{r}) | i_p \rangle \gamma^\mu (1 - x\gamma^5) \langle f_n | \hat{\psi}_n(\mathbf{r}) | i_n \rangle \right] \times \\ \left[ \langle f_e | \hat{\psi}_e(\mathbf{r}) | i_e \rangle \gamma_\mu (1 - \gamma^5) \langle f_\nu | \hat{\psi}_\nu(\mathbf{r}) | 0_\nu \rangle \right] + \text{c.c.} \\ = \frac{G_F}{\sqrt{2}} \langle f_{p,n} | J_{\text{had}}^\mu | i_{p,n} \rangle \langle f_{e,\nu} | J_{\mu}^{\text{lep}} | i_{e,\nu} \rangle, \quad (10)$$

where  $|i\rangle = |i_{p,n}\rangle \otimes |i_{e,\nu}\rangle$ ,  $|f\rangle = |f_{p,n}\rangle \otimes |f_{e,\nu}\rangle$  and the hadronic and leptonic terms can be further factorised as follows:

$$|i_{p,n}\rangle = |i_p\rangle \otimes |i_n\rangle, \quad |f_{p,n}\rangle = |f_p\rangle \otimes |f_n\rangle, \quad (11)$$

$$|i_{e,\nu}\rangle = |i_e\rangle \otimes |0_\nu\rangle, \quad |f_{e,\nu}\rangle = |f_e\rangle \otimes |f_\nu\rangle. \quad (12)$$

This is due to the independent-particle nuclear shell model adopted here and the fact that neutrinos do not interact electromagnetically with fermions and can therefore be safely considered free. In Eq. (10) we have also defined the leptonic

$$J_{\text{lep}}^\mu = \hat{\psi}_e(\mathbf{r}) \gamma^\mu (1 - \gamma^5) \hat{\psi}_\nu(\mathbf{r}), \quad (13)$$

and hadronic currents

$$J_{\text{had}}^\mu = \hat{\psi}_p(\mathbf{r}) \gamma^\mu (1 - x\gamma^5) \hat{\psi}_n(\mathbf{r}). \quad (14)$$

This separation allows the nuclear matrix element  $\langle f_{p,n} | \dots | i_{p,n} \rangle$  (which includes the Fermi and Gamow-Teller (GT) contributions) to be treated independently of the lepton wave functions  $\langle f_{e,\nu} | \dots | i_{e,\nu} \rangle$ .

A general expression for the field operators of the initial and final fermionic states, characterised by both a continuum and a discrete spectrum and appearing in the transition operator matrix element (10), can be written as follows:

$$\hat{\psi}_i(\mathbf{r}) = \sum_\phi \left[ \langle \mathbf{r} | \phi \rangle \hat{c}_{d,i} + \langle \phi | \mathbf{r} \rangle \hat{d}_{d,i}^\dagger \right] \\ + \int d\mathbf{k} \sum_l \left[ \langle \mathbf{r} | \mathbf{k}, \mathbf{l} \rangle \hat{c}_{c,i} + \langle \mathbf{k}, \mathbf{l} | \mathbf{r} \rangle \hat{d}_{c,i}^\dagger \right] \quad (15)$$

where

- $\phi$  is a set of wave functions labelled by suitable quantum numbers with a discrete spectrum (for example, total angular momentum  $j$  and principal quantum number  $n$ ).
- $\hat{c}_{d,i}$  and  $\hat{d}_{d,i}^\dagger$  are the fermion annihilation operator and the antifermion creation operator for the discrete spectrum states, respectively.
- $\mathbf{k}$  is a set of continuum quantum numbers (such as energy for a free particle), and  $\mathbf{l}$  is a set of discrete spectrum quantum numbers.
- $\hat{c}_{c,i}$  and  $\hat{d}_{c,i}^\dagger$  are the fermion annihilation operator and the antifermion creation operator for the continuum spectrum states, respectively.

Similarly, for the final state  $f$ , we have the field operator  $\hat{\psi}_f^\dagger$ :

$$\hat{\psi}_f^\dagger(\mathbf{r}) = \sum_\phi \left[ \langle \phi | \mathbf{r} \rangle \hat{c}_{d,f}^\dagger + \langle \mathbf{r} | \phi \rangle \hat{d}_{d,f} \right] \\ + \int d\mathbf{k} \sum_l \left[ \langle \mathbf{k}, \mathbf{l} | \mathbf{r} \rangle \hat{c}_{c,f}^\dagger + \langle \mathbf{r} | \mathbf{k}, \mathbf{l} \rangle \hat{d}_{c,f} \right]. \quad (16)$$

Using expressions (15) and (16), we can construct the field operators that appear in the hadronic and leptonic currents in Eqs. (13) and (14), respectively. Here, we are interested in EC, AC, and  $\beta^+$  decay, which involve (free) neutrinos, continuum electrons and positrons, as well as bound protons, neutrons, and electrons.

**Electron capture** In EC, the annihilation of an electron results in the formation of a bound neutron and a neutrino, which interacts very weakly with matter and can therefore be considered free. Thus, only the continuum spectrum part of (16) needs to be retained. Neutrinos are identified by their relativistic kinetic energy  $W_\nu$ , their total angular momentum  $K_\nu$ , and the projection of this angular momentum along a quantization axis  $M_\nu$

$$\hat{\psi}_\nu^\dagger(\mathbf{r}) = \int dW_\nu \sum_{K_\nu, M_\nu} \left[ \langle W_\nu, K_\nu, M_\nu | \mathbf{r} \rangle \hat{c}_{\nu,c}^\dagger + \langle \mathbf{r} | W_\nu, K_\nu, M_\nu \rangle \hat{d}_{\nu,c} \right]. \quad (17)$$

The decaying Be atom can be partially or fully ionised due to the high BBN temperature; therefore, for the electron field operator, we must retain both the discrete ( $n, j$ , even if only the  $s$ -symmetry orbitals have finite overlap with the nucleus) and continuum ( $W_c$ ) energy spectrum components:

$$\hat{\psi}_e(\mathbf{r}) = \sum_{n,j} \left[ \langle \mathbf{r} | n, j \rangle \hat{c}_{d,i} + \langle n, j | \mathbf{r} \rangle \hat{d}_{d,i}^\dagger \right] + \int dW_c \sum_{K_c, M_c} \left[ \langle \mathbf{r} | W_c, K_c, M_c \rangle \hat{c}_{e,c} + \langle W_c, K_c, M_c | \mathbf{r} \rangle \hat{d}_{e,c}^\dagger \right]. \quad (18)$$

In addition, neutrons ( $n$ ) and protons ( $p$ ) are in bound states within the parent and daughter nuclei, so the continuum spectrum must be excluded. Considering the symmetries of the system, we must use the quantum numbers associated with  $\hat{J}^2$  and  $\hat{J}_z$ , which we denote as  $j_{p,n}$  and  $M_{p,n}$ :

$$\begin{aligned} \hat{\psi}_p(\mathbf{r}) &= \sum_{j_p, M_p, \xi_p} \left[ \langle \mathbf{r} | j_p, M_p, \xi_p \rangle \hat{c}_p + \langle j_p, M_p, \xi_p | \mathbf{r} \rangle \hat{d}_p^\dagger \right] \\ \hat{\psi}_n^\dagger(\mathbf{r}) &= \sum_{j_n, M_n, \xi_n} \left[ \langle j_n, M_n, \xi_n | \mathbf{r} \rangle \hat{c}_n^\dagger + \langle \mathbf{r} | j_n, M_n, \xi_n \rangle \hat{d}_n \right] \end{aligned} \quad (19)$$

where the quantum numbers  $\xi_{p,n}$  define the discrete energy of the state of the nucleon.

**$\bar{\nu}$ -capture** Field operators are the same as for EC, but both the antineutrino

$$\langle W_\nu, K_\nu, M_\nu | \mathbf{r} \rangle, \quad (20)$$

and positron wave functions

$$\langle \mathbf{r} | W_c, K_c, M_c \rangle \quad (21)$$

must be negative energy solutions of the Dirac equation.

**$\beta^+$  decay** For  $\beta^+$  decay, the field operators are the same as for EC and AC, but a positron in the continuum spectrum is created. Therefore, the wave function of the positron,

$$\langle \mathbf{r} | W_c, K_c, M_c \rangle \quad (22)$$

must also be a negative energy solution of the Dirac equation.

#### 4. From field operators to wave functions

In this section, we derive the explicit form of the matrix elements appearing in Eq. (10), when the field operators have the general form given in Eqs. (15) and (16). Specifically, for EC,  $\beta^+$  decay, and AC, the relevant field operators are those introduced in Eqs. (17)-(22). The calculation proceeds in three main steps:

- We formulate the appropriate Dirac equation and select a convenient basis of single-particle wave functions.
- We solve the Dirac equation using a DHF approach to obtain the antisymmetric many-body wave functions for both nucleons and electrons.
- The resulting wave functions are substituted into the field operators to compute the required matrix elements.

##### 4.1. Dirac formalism in the context of leptonic and hadronic currents for a central potential

In the two-component representation, the Dirac spinor is written as

$$\psi(\mathbf{x}) = \begin{pmatrix} \psi_u(\mathbf{x}) \\ \psi_d(\mathbf{x}) \end{pmatrix}, \quad (23)$$

where the upper ( $u$ ) and lower ( $d$ ) components correspond to the large and small components in the Dirac representation. Each component contains the spin degrees of freedom, which are included in the variable  $\mathbf{x}$  together with the spatial coordinates.

The time-independent Dirac equation in matrix form reads

$$\begin{pmatrix} mc^2 + V(\mathbf{x}) & c \boldsymbol{\sigma} \cdot \mathbf{p} \\ c \boldsymbol{\sigma} \cdot \mathbf{p} & -mc^2 + V(\mathbf{x}) \end{pmatrix} \begin{pmatrix} \psi_u(\mathbf{x}) \\ \psi_d(\mathbf{x}) \end{pmatrix} = E \begin{pmatrix} \psi_u(\mathbf{x}) \\ \psi_d(\mathbf{x}) \end{pmatrix}, \quad (24)$$

where  $V(\mathbf{x})$  is, in this case, a central potential,  $m$  is the particle's rest mass,  $\mathbf{p}$  its momentum, and  $\boldsymbol{\sigma}$  is the vector of Pauli matrices  $[\sigma_x, \sigma_y, \sigma_z]$ .

Owing to the spherical symmetry of the interaction potential, the states are classified by the quantum numbers  $(n, \kappa, j, M)$ , where  $n$  is the radial (principal) quantum number and  $\kappa$  is the Dirac angular quantum number, which is defined through

$$\hat{K} \psi(\mathbf{x}) = -\hbar \kappa \psi(\mathbf{x}), \quad (25)$$

where

$$\hat{K} = \hbar \gamma_0 \left( 2 \hat{\mathbf{S}} \cdot \hat{\mathbf{J}} - \frac{1}{2} \right), \quad (26)$$

$j$  is the eigenvalue of the total angular momentum operator  $\hat{J}$ , and  $M$  is its projection onto the arbitrarily chosen quantisation axis, since in relativistic quantum mechanics neither the angular momentum  $\hat{\mathbf{L}}$  nor the spin  $\hat{\mathbf{S}}$  is separately conserved. From the commutation with the Hamiltonian in Eq. (24),  $[\hat{H}, \hat{K}] = 0$ , the associated quantum number  $\kappa$  acquires two possible values for each total angular momentum  $j$ , determining the orbital angular momentum of the upper and lower components as

$$\kappa = \pm \left( j + \frac{1}{2} \right) \Rightarrow \begin{aligned} l_u &= j \pm \frac{1}{2}, \\ l_d &= j \mp \frac{1}{2}. \end{aligned} \quad (27)$$

The spinor in Eq. (23) can be factorized into radial and angular-spin components:

$$\psi_u(\mathbf{x}) = U(r) \mathcal{Y}_M^{j, l_u}(\theta, \phi), \quad (28)$$

$$\psi_d(\mathbf{x}) = i D(r) \mathcal{Y}_M^{j, l_d}(\theta, \phi), \quad (29)$$

where the angular-spin function is defined as

$$\mathcal{Y}_M^{j, l}(\theta, \phi) = \sum_{l_z, s_z} \langle l l_z, s s_z | j M \rangle Y_l^{l_z}(\theta, \phi) \chi_s^{s_z}. \quad (30)$$

By introducing the reduced radial functions  $u(r) = rU(r)$  and  $d(r) = rD(r)$ , we obtain

$$\psi(\mathbf{x}) = \begin{pmatrix} \frac{u(r)}{r} \mathcal{Y}_M^{j,l_u}(\Omega) \\ i \frac{d(r)}{r} \mathcal{Y}_M^{j,l_d}(\Omega) \end{pmatrix}. \quad (31)$$

The Dirac equation for the radial components then becomes:

$$\begin{pmatrix} V(r) + mc^2 & -\hbar c \frac{d}{dr} + \hbar c \frac{\kappa}{r} \\ \hbar c \frac{d}{dr} + \hbar c \frac{\kappa}{r} & V(r) - mc^2 \end{pmatrix} \begin{pmatrix} u_\kappa(r) \\ d_\kappa(r) \end{pmatrix} = E \begin{pmatrix} u_\kappa(r) \\ d_\kappa(r) \end{pmatrix}. \quad (32)$$

#### 4.2. Choice of scalar and vector potentials

More general potentials (pseudoscalar, axial vector, tensor, etc.) could be introduced, but for our purposes it is sufficient to consider suitable combinations of scalar and vector potentials when modelling hadronic or leptonic currents. Moreover, we assume a mean-field approximation of the nuclear and electron potentials; that is, we assume an ansatz for the solution of the general Dirac equation (32). In particular, the key assumption is that the many-electron or many-nucleon wave function is represented by a Slater determinant of four-component Dirac spinors, so the total electron or nuclear density  $\rho(\mathbf{x})$  is constructed from these relativistic orbitals. Each orbital represents an independent particle moving in an average potential, which must be calculated self-consistently and inherently includes electron-positron (large/small component) or nucleon-antinucleon mixing (Morresi et al. 2018).

**Nucleons** For nucleons, we use the independent-particle model within the relativistic Woods-Saxon phenomenological representation of the nuclear potential (Schwierz et al. 2007). In this context, within relativistic mean-field theory, the effective single-particle potential experienced by a nucleon is described as the sum of a Lorentz-scalar attractive field,  $V_s(r)$ , generated by  $\sigma$ -meson exchange, and a Lorentz-vector repulsive field,  $V_v(r)$ , associated with  $\omega$ -meson exchange. The Dirac Hamiltonian couples to the combinations  $V_v(r) \pm V_s(r)$ , which determine the dynamics of the upper and lower components of the Dirac spinor.

These combinations reproduce the depth of the central Woods-Saxon potential (Morresi et al. 2018):

$$V_{\text{nuc}}(r) = -\frac{V}{1 + \exp\left(\frac{r - R_N}{a}\right)}, \quad (33)$$

where  $a$  is the diffuseness parameter, which controls how rapidly the potential falls off at the nuclear surface. Here,  $R_N = R_0 A^{1/3}$  is the nuclear radius, with  $A = N + Z$  the mass number, given by the sum of the atomic number ( $Z$ ) and the number of neutrons ( $N$ ), and  $R_0 = 1.25$  fm, consistent with empirical nuclear charge radii. The depth

$$V = V_0 \left(1 \pm \chi \frac{N - Z}{A}\right),$$

incorporates isospin dependence, with the + sign for protons and the - sign for neutrons, where  $V_0 = 45\text{--}55$  MeV is a constant and  $\chi$  is an isospin-asymmetry coefficient ( $\approx 0.6\text{--}0.9$ ). The mixture of scalar and vector terms also accounts for the spin-orbit

splitting

$$V_{\text{SO}}(r) = \frac{\tilde{V}}{1 + \exp\left(\frac{r - \tilde{R}_N}{a}\right)}, \quad (34)$$

where  $\tilde{V} = \tilde{\lambda}V$  is the spin-orbit strength ( $\tilde{\lambda} \approx 20\text{--}25$ ), and  $\tilde{R}_N = \tilde{R}_0 A^{1/3}$  is the spin-orbit radius ( $\tilde{R}_0 \approx R_0$ ).

Thus, the Woods-Saxon nuclear mean-field potential must be regarded as a combination of scalar and vector components:

$$\begin{aligned} V_{\text{nuc}}(r) &= V_v(r) + V_s(r) = -\frac{V}{1 + \exp\left(\frac{r - R_N}{a}\right)}, \\ V_{\text{SO}}(r) &= V_v(r) - V_s(r) = \frac{\tilde{V}}{1 + \exp\left(\frac{r - \tilde{R}_N}{a}\right)}, \end{aligned} \quad (35)$$

which leads to the following form of the Dirac matrix in the secular equation for nuclear matter:

$$\begin{pmatrix} V_v(r) + V_s(r) + mc^2 & -\hbar c \frac{d}{dr} + \hbar c \frac{\kappa}{r} \\ \hbar c \frac{d}{dr} + \hbar c \frac{\kappa}{r} & V_v(r) - V_s(r) - mc^2 \end{pmatrix}, \quad (36)$$

where  $m$  is the rest mass of the proton ( $m_p$ ) or the neutron ( $m_n$ ).

**Leptons** Electrons move in the Coulomb field of the nucleus and the other electrons, and experience a non-local electron-electron interaction. In the DHF method, this interaction is approximated by the following local potentials (Morresi et al. 2018; Taioli & Simonucci 2021):

$$\begin{aligned} V_{\text{Coul}}(r) &= -\frac{Z}{r}, \\ V_{\text{Hartree}}(r) &= \int d^3 r' \frac{\rho(r')}{r_{>}}, \quad r_{>} = \max(r, r'), \\ V_{\text{Fock}}(r) &= \frac{9}{4} \left(\frac{3}{\pi} \rho(r)\right)^{1/3}, \end{aligned} \quad (37)$$

yielding the total electronic potential

$$V_{\text{el}}(r) = V_{\text{Coul}}(r) + V_{\text{Hartree}}(r) - V_{\text{Fock}}(r), \quad (38)$$

where  $V_{\text{Coul}}$  is the electron-nuclear attraction, and  $V_{\text{Hartree}}$  and  $V_{\text{Fock}}$  are the classical Coulomb and exchange terms representing electron-electron repulsion within the HF approximation to the many-body potential. This is essentially a local density approximation (LDA) of the electron-electron correlation potential. Since the electromagnetic interaction is vectorial, the Dirac operator for electrons reduces to

$$\begin{pmatrix} V_{\text{el}}(r) + m_e c^2 & -\hbar c \frac{d}{dr} + \hbar c \frac{\kappa}{r} \\ \hbar c \frac{d}{dr} + \hbar c \frac{\kappa}{r} & V_{\text{el}}(r) - m_e c^2 \end{pmatrix}, \quad (39)$$

where  $m_e$  is the electron rest mass.

**Neutrinos** Neutrinos are treated as free particles; their wave functions are therefore eigenstates of the Dirac operator without a potential:

$$\begin{pmatrix} 0 & -\hbar c \frac{d}{dr} + \hbar c \frac{\kappa}{r} \\ \hbar c \frac{d}{dr} + \hbar c \frac{\kappa}{r} & 0 \end{pmatrix}. \quad (40)$$

### 4.3. Numerical solution of the Dirac equation

The general Dirac equation (32) can be adapted to the specific cases of EC and AC, provided that the nucleonic and leptonic single-particle wave functions required for the transition matrix elements are calculated by solving Eqs. (36), (39), and (40). The numerical strategy used to solve Eq. (32) involves finite-difference diagonalisation. These methodologies are described in the appendix A.

## 5. Electron and neutrino capture rates during the NSE epoch

### 5.1. ${}^7\text{Be}$ and ${}^7\text{Li}$ nuclear shell configurations

EC on  ${}^7\text{Be}$  occurs through two GT transitions connecting  ${}^7\text{Be}$  to states of  ${}^7\text{Li}$  (we label 0 as the nuclear ground state of Li, 1 as its nuclear excited state, and  ${}^*$  indicates decay from the excited state of Be). Under Earth conditions,  ${}^7\text{Be}$  decays from the ground state ( $3/2^-$ ) via EC (see reaction (2) and Fig. (1) for the decay scheme) into the ground state of  ${}^7\text{Li}$  ( $3/2^-$ ) with a half-life of 53 days in 89.7% of cases and a  $Q$ -value  $Q_0 = 861.815$  keV. In 10.3% of cases ( $Q_0 = 384.215$  keV), it decays to the first ex-

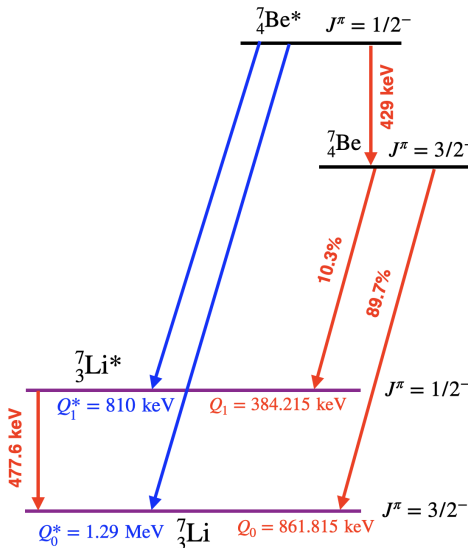


Fig. 1:  ${}^7\text{Be}$  electron capture decay scheme. The  $Q$ -values and branching ratios for the four decay channels are also provided (0 =  ${}^7\text{Li}$  nuclear ground state, 1 =  ${}^7\text{Li}$  nuclear excited state,  ${}^*$  indicates decay from the excited state of  ${}^7\text{Be}$ ).

cited state ( $1/2^-$ ) of  ${}^7\text{Li}$ . Both are allowed transitions; the former is a mixed Fermi and GT transition, while the latter is purely GT ( $\Delta J = 1$ , no parity change).

In the astrophysical environment under the NSE conditions considered here, we must also account for the possibility that  ${}^7\text{Be}$  is thermally excited to its first excited state at  $E_{{}^7\text{Be}}^* = 0.429$  MeV, characterised by the quantum number  $J^\pi = 1/2^-$  (see Fig. (1)). This excited state of  ${}^7\text{Be}$  lies at an excitation energy sufficiently close to the temperature  $k_B T \simeq 0.1$  MeV, at which this nucleus is synthesised during BBN, to be populated. From this state, the capture can proceed to either the ground state or the first excited state of  ${}^7\text{Li}$  (see Fig. (1)). The transition from  ${}^7\text{Be}^*(1/2^-)$  to the ground state of  ${}^7\text{Li}$  ( $J^\pi = 3/2^-$ ) is an allowed GT transition. Due to the additional excitation energy of the parent nucleus,

the corresponding  $Q$ -value increases to  $Q_0^* \approx 1.29$  MeV. Capture to the first excited state of  ${}^7\text{Li}$  at 0.478 MeV ( $J^\pi = 1/2^-$ ) is a superallowed GT transition ( $\Delta J = 0$ , no parity change), with a reduced  $Q$ -value  $Q_1^* \simeq 0.81$  MeV. For both these transitions from  ${}^7\text{Be}^*$ , the EC decay proceeds entirely via the GT operator, as Fermi transitions are forbidden by isospin selection rules in the  $A = 7$  system. The enhancement of the  $Q$ -value for captures originating from the excited state directly affects the phase space available for the emitted neutrino and thus modifies the total EC rate in a temperature-dependent manner, especially in environments where the population of the 0.429 MeV level becomes non-negligible. Since  $Q_{0,1}^* > m_e$ , excitation of this nuclear level in  ${}^7\text{Be}$  may allow positron emission (see reaction (3)) via this excited state. We also note that the thermal population of the  $1/2^-$  state is

$$P_1 \simeq \frac{2J+1}{\mathcal{Z}} e^{-E^*/(k_B T)} \simeq \frac{1}{2} e^{-0.4292/(k_B T)}, \quad (41)$$

where we approximate the partition function  $\mathcal{Z}$  by the ground-state degeneracy. At  $k_B T \simeq 0.1$  MeV,  $P_1 \sim 1\%$ . Furthermore, an antineutrino threshold of  $E_\nu^{\text{th}} = 0$  applies, although this is less favourable than decay from the ground state. Most importantly, in addition to this population factor, it is necessary to determine how the EC and AC or  $\beta^+$  decay rate from  ${}^7\text{Be}^*$  compares to that of  ${}^7\text{Be}$  in its ground state, to assess whether all weak processes involving this excited state contribute significantly or only marginally to the overall  ${}^7\text{Be}$  destruction rate during BBN. Finally, we also note that  $\bar{\nu}_e$ -capture and  $e^-$ -capture transitions to the first excited state of  ${}^7\text{Li}$  are allowed, but their  $Q$ -values are less favourable.

To calculate the matrix element in Eq. (10), we must specify the initial and final configurations on which the weak interaction potential  $V$  acts. This requires knowledge of the wave functions of the states involved in the electro-nuclear transition, namely, the nuclear and atomic shell configurations of both  ${}^7\text{Be}$  and  ${}^7\text{Li}$ . Within the nuclear shell model, the low-lying level structure of  ${}^7\text{Be}$  and  ${}^7\text{Li}$  is described as a closed  $1s_{1/2}$  shell with three valence nucleons in the  $1p_{3/2}$  shell (see Fig. (2)). In particular:

–  **${}^7\text{Be}$**  (left side of Fig. (2)). The nucleus contains four protons and three neutrons. Two protons and two neutrons fill the  $1s_{1/2}$  closed shell with total spin-parity  $J = 0^+$ . In the incomplete  $1p_{3/2}$  subshell, the remaining two protons tend to pair off to total angular momentum  $J_p = 0$ , while the remaining unpaired neutron carries  $j_n = 3/2$ . As the  $p$ -shell has negative parity, the ground state is  $J^\pi = 3/2^-$ . In our simulations, we therefore assume a core with  $J_C = 0$  that couples geometrically with the remaining neutron and essentially acts as a spectator for the transition.

–  **${}^7\text{Li}$**  (right side of Fig. (2)). The level scheme is analogous to that of  ${}^7\text{Be}$ , with the only difference being that the unpaired nucleon in the  $1p_{3/2}$  orbital is a proton. Consequently, the ground state is also  $J^\pi = 3/2^-$ .

Similar considerations apply to determining the symmetry of the excited nuclear levels of  ${}^7\text{Be}$  and  ${}^7\text{Li}$ , which result from the promotion of a neutron to the  $1p_{1/2}$  nuclear level (see red arrows in Fig. (2)). These configurations are consistent with the observed level scheme and standard independent-particle shell model predictions, resulting in the ground and first excited states (both  $1/2^-$ ) shown in Fig. (1). Unpaired nucleons of opposite isospin tend to couple to the maximum total angular momentum; in this context,  $J_C = 3$  is the physically realised value, which we denote as the core-coupling angular momentum. At even higher excita-

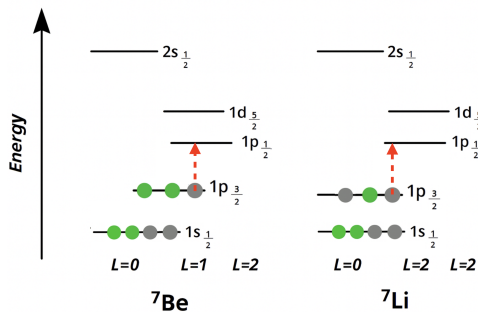


Fig. 2: Shell model configurations of the ground state of  ${}^7\text{Be}$  (left,  $3/2^-$ ) and  ${}^7\text{Li}$  (right,  $3/2^-$ ). Green dots represent protons and grey dots represent neutrons. Also shown are the excited nuclear states of  ${}^7\text{Be}$  (left,  $1/2^-$ ) and  ${}^7\text{Li}$  (right,  $1/2^-$ ), which result from the promotion of a neutron to the  $1p_{1/2}$  nuclear level (red arrows).

tion energies, the pure shell model picture becomes less reliable, and significant configuration mixing is expected. Nevertheless, for the weak processes of interest, the relevant matrix elements are dominated by transitions involving the valence nucleons in the  $1p$  shell.

### 5.2. Electron and antineutrino capture rate

For EC or AC on  ${}^7\text{Be}$ , four single-particle transitions may be considered:

- ${}^7\text{Be}$  ground state to  ${}^7\text{Li}$  ground state:  $p(1p_{3/2}) \rightarrow n(1p_{3/2})$ ;
- ${}^7\text{Be}$  excited state to  ${}^7\text{Li}$  ground state:  $p(1p_{1/2}) \rightarrow n(1p_{3/2})$ ;
- ${}^7\text{Be}$  excited state to  ${}^7\text{Li}$  excited state:  $p(1p_{1/2}) \rightarrow n(1p_{1/2})$ ;
- ${}^7\text{Be}$  ground state to  ${}^7\text{Li}$  excited state:  $p(1p_{3/2}) \rightarrow n(1p_{1/2})$ .

In all cases, a proton is converted into a neutron, while two nucleons (one proton and one neutron) remain as spectators in the  $p$  shell.

Within our ab initio framework, the decay rate per  ${}^7\text{Be}$  nucleus is obtained using Eq. (7), where DHF calculations of the initial and final state nuclear and electronic wave functions are performed and substituted into the weak leptonic and hadronic currents in Eq. (10). Additionally, this rate must be multiplied by the initial and final population factors and projectile densities, also taking into account the temperature through the chemical potentials. In particular, the electron, positron, and relic antineutrino population factors can be obtained via Fermi–Dirac distributions, each with its own temperature, as follows:

$$f_{e^\pm}(E, T, \mu_e) = \frac{1}{1 + e^{\frac{E \pm \mu_e}{k_B T}}}, \quad (42)$$

$$f_\nu(E, T_\nu) = \frac{1}{1 + e^{\frac{E}{k_B T_\nu}}},$$

where  $T_\nu$  is the relic (anti-)neutrino temperature calculated in Eq. (B.25) of the Appendix (recall that we assume  $\mu_\nu = \mu_{\bar{\nu}} = 0$ ; see section (B.5) of the Appendix), while electrons are in thermal equilibrium with photons, so  $T = T_\gamma$  is the usual photon temperature, and  $\mu_e$  is the electron chemical potential. Moreover, after the transition, the final neutrino must occupy a free state. Therefore, the required neutrino population factor is

$$g_\nu(E, T_\nu) = 1 - f_\nu(E, T_\nu) = 1 - \frac{1}{1 + e^{\frac{E}{k_B T_\nu}}}. \quad (43)$$

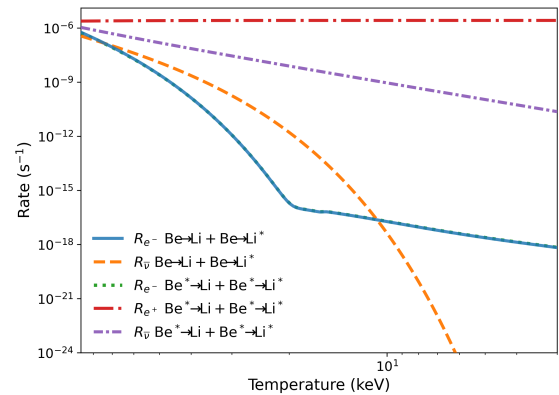


Fig. 3: Electron ( $R_{e^-}$ ), positron ( $R_{e^+}$ ), and antineutrino ( $R_\nu$ ) capture rates for the  ${}^7\text{Be} \rightarrow {}^7\text{Li}$  transitions are shown as a function of temperature (logarithmic and inverted). Only rates greater than  $10^{-24} \text{ s}^{-1}$  are displayed.  $\text{Be}^*$  and  $\text{Li}^*$  denote the excited states of Be and Li, respectively.

The chemical potential of the electrons can be obtained by inverting Eq. (B.29) for a given proton density, assuming charge neutrality of the Universe and following the procedure explained in Appendix B.4.

The total rate for EC is obtained by integrating over all energies:

$$\lambda_{\text{EC}}(T) = \int_0^\infty \Gamma(E) f_{e^-}(E, T, \mu_e) g_\nu(E, T_\nu) dE. \quad (44)$$

Moreover, the AC rate is

$$\lambda_{\text{AC}}(T) = \int_{-\infty}^0 \Gamma(E) [1 - f_{e^+}(E, T, \mu_e)] f_\nu(E, T_\nu) dE. \quad (45)$$

The integrals (44) and (45) have been evaluated in the temperature range relevant after NSE freeze-out ( $10 \text{ keV} < k_B T < 100 \text{ keV}$ ). Finally, the total weak capture rate of  ${}^7\text{Be}$  is

$$\lambda_{\text{weak}}(T) = \lambda_{\text{EC}}(T) + \lambda_{\text{AC}}(T), \quad (46)$$

which is evaluated numerically as a function of temperature (or cosmic time). A similar concept applies when determining the decay rates of excited nuclear states, where the relevant population factors follow a Boltzmann distribution as in Eq. (41). For positron emission, similar calculations are required, but with positron kinematics replacing those of the captured electron or antineutrino. Finally, the total rate is the sum of the independent rates for the ground and excited nuclear states for all possible weak reactions. The results are listed in Tab.(1) and shown in Fig.(3). Additionally, Tables (C.1), (C.2), (C.3), and (C.4) in the Appendix present the results specific to each transition type (EC, positron decay, and AC) and nuclear level (ground or excited states of Be and Li). We observe that the contribution of  $\bar{\nu}_e$ -capture becomes more significant compared to EC as temperature decreases (or time increases), while positron emission, which occurs only from the  ${}^7\text{Be}$  excited nuclear state, remains roughly constant with temperature. However, we emphasise that even 3 s after the Big Bang, corresponding to a temperature of 87.23 keV, the EC half-life of  ${}^7\text{Be}$  is approximately 1.5 days, which is too long compared to the synthesis of primordial  ${}^7\text{Li}$ , believed to have occurred within the first 1000 s of the Universe's existence. Nevertheless, we note that our assessment from first-principles is significantly closer to the expected half-life than previous simulations based on  $\log(ft)$  systematics in the NSE temperature range (Fuller & Smith 2010), which estimated it at approximately 10 days.

Table 1: 3rd and 4th columns: electron ( $R_{e^-}$ ) and antineutrino ( $R_{\bar{\nu}}$ ) capture rates from  ${}^7\text{Be}$  (ground) to  ${}^7\text{Li}$  (ground) and  ${}^7\text{Li}^*$  (excited nuclear state) as a function of time in seconds since the Big Bang (1st column) or temperature in keV (2nd column). 5th, 6th, and 7th columns: electron ( $R_{e^-}$ ), positron ( $R_{e^+}$ ), and antineutrino ( $R_{\bar{\nu}}$ ) capture rates from  ${}^7\text{Be}^*$  (excited nuclear state) to  ${}^7\text{Li}$  (ground) and  ${}^7\text{Li}^*$  (excited nuclear state). Last column: total rate ( $R_{\text{tot}}$ ). Rates are given in units of  $\text{s}^{-1}$ .

$t$ (s)	$k_B T$ (keV)	$R_{e^-}$ $\text{Be} \rightarrow (\text{Li} + \text{Li}^*)$	$R_{\bar{\nu}}$ $\text{Be} \rightarrow (\text{Li} + \text{Li}^*)$	$R_{e^-}$ $\text{Be}^* \rightarrow (\text{Li} + \text{Li}^*)$	$R_{e^+}$ $\text{Be}^* \rightarrow (\text{Li} + \text{Li}^*)$	$R_{\bar{\nu}}$ $\text{Be}^* \rightarrow (\text{Li} + \text{Li}^*)$	$R_{\text{tot}}$
3.156	87.23	5.878e-07	3.633e-07	5.480e-07	2.445e-06	1.093e-06	5.037e-06
7.964	54.91	7.583e-09	2.322e-08	7.375e-09	2.581e-06	2.112e-07	2.830e-06
20.10	34.57	1.432e-11	6.774e-10	1.429e-11	2.637e-06	4.530e-08	2.683e-06
50.72	21.76	1.241e-15	5.047e-12	1.257e-15	2.656e-06	1.030e-08	2.666e-06
127.99	13.70	4.872e-17	3.943e-15	4.983e-17	2.661e-06	2.420e-09	2.663e-06
322.99	8.623	1.175e-17	9.683e-16	1.209e-17	2.662e-06	5.806e-10	2.663e-06
815.07	5.428	2.977e-18	2.464e-16	3.073e-18	2.663e-06	1.413e-10	2.663e-06
2056.9	3.417	9.238e-19	7.652e-17	9.553e-19	2.663e-06	3.468e-11	2.663e-06
5190.6	2.151	3.065e-19	2.544e-17	3.174e-19	2.663e-06	8.565e-12	2.663e-06
13099	1.354	9.851e-20	8.186e-18	1.021e-19	2.663e-06	2.124e-12	2.663e-06
31560	0.8723	3.725e-20	3.097e-18	3.862e-20	2.663e-06	5.665e-13	2.664e-06

## 6. Proton capture on ${}^7\text{Be}$

The reaction  ${}^7\text{Be}(p, \gamma){}^8\text{B}$  at BBN energies is dominated by non-resonant direct capture, primarily populating the  ${}^8\text{B}$  ground state ( $J^\pi = 2^+$ ) with a  $Q$ -value of 137 keV. Higher-lying resonant states (at approximately 769.5 keV) are at too high an energy for proton kinetic energies below NSE and therefore contribute only subdominantly. A diagram of the nuclear levels involved in this reaction is shown in Fig. (4).

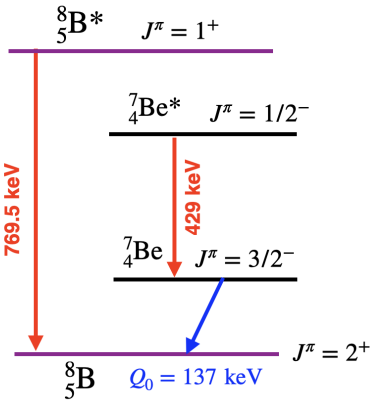


Fig. 4:  ${}^7\text{Be}$  proton capture decay scheme. The  $Q$ -value for the only decay channel considered here (ground-to-ground state decay) is also provided (0 = nuclear ground state, \* indicates the excited states of  ${}^7\text{Be}$  and  ${}^8\text{B}$ ).

In this context, we note that the photon carries away angular momentum 1. At the low energies relevant for BBN, this reaction proceeds predominantly via electric E1 dipole transitions from incoming  $s$ -wave protons, due to the absence of a centrifugal barrier for  $l = 0$ , with a subleading contribution from  $d$ -wave capture to the bound  $p_{3/2}$  configuration of  ${}^8\text{B}$ . The  $s$ -wave to  $p$ -shell bound state transition, together with the selection rules (parity change  $\Delta\pi = -1$  and  $\Delta l = \pm 1$ ), leads to a  $2^+$  nuclear ground state of  ${}^8\text{B}$ .

### 6.1. Radiative capture ${}^7\text{Be}(p, \gamma){}^8\text{B}$ : classical approach

We have analysed two types of PC, as reported in (5) and (6). Because the first excited state of  ${}^8\text{B}$  lies at 770 keV, well above

the reaction  $Q$ -value ( $Q \simeq 137$  keV), PC at astrophysical energies can populate only the ground state of  ${}^8\text{B}$ . Thus, in these reactions, almost the entire  $Q$ -value (137 keV) is carried away by the emitted photon, while the recoil energy of the  ${}^8\text{B}$  nucleus is negligible ( $< 1$  keV).

For these reactions, we must determine the corresponding cross-sections, from which we can, in principle, obtain the nuclear decay rate of  ${}^7\text{Be}$  by multiplying by the proton flux (number of protons per unit area per unit time).

The thermally averaged reaction rate per particle pair per unit volume can be determined by considering protons and Be nuclei as classical particles, that is their velocities  $v_p, v_{\text{Be}}$  are distributed according to the following Maxwell-Boltzmann distribution

$$f(v_i) = 4\pi \left( \frac{m_i}{2\pi k_B T} \right)^{3/2} v_i^2 \exp\left(-\frac{m_i v_i^2}{2k_B T}\right), \quad (47)$$

where  $v_i = v_{\text{Be}}$ ,  $m_i = m_{\text{Be}}$  or  $v_i = v_p$ ,  $m_i = m_p$  are the velocities and masses of Be and  $p$ , respectively, and  $T$  is the plasma temperature. As each proton and Be nucleus has a different momentum, we must integrate over all possible momenta.

The PC rate ( $R_{\text{PC}}$ ) per target particle of Be per unit volume is therefore given by

$$\begin{aligned} R_{\text{PC}} &= n_p^{\text{free}}(T) \int \frac{m_p^3 d^3 v_p}{(2\pi m_p k_B T)^{3/2}} \int \frac{m_{\text{Be}}^3 d^3 v_{\text{Be}}}{(2\pi m_{\text{Be}} k_B T)^{3/2}} e^{-\frac{m_p v_p^2}{2k_B T} - \frac{m_{\text{Be}} v_{\text{Be}}^2}{2k_B T}} v_{\text{rel}} \sigma(v_{\text{rel}}) \\ &= n_p^{\text{free}}(T) \frac{(m_p m_{\text{Be}})^{3/2}}{(2\pi k_B T)^3} \int d^3 v_{\text{rel}} \int d^3 V_{\text{CM}} e^{-\frac{M V_{\text{CM}}^2}{2k_B T} - \frac{\mu_{\text{rel}}^2}{2k_B T}} v_{\text{rel}} \sigma(v_{\text{rel}}) \\ &= n_p^{\text{free}}(T) \left( \frac{m_p m_{\text{Be}}}{m_p + m_{\text{Be}}} \right)^{3/2} \frac{1}{(2\pi k_B T)^{3/2}} \int d^3 v_{\text{rel}} e^{-\frac{\mu_{\text{rel}}^2}{2k_B T}} v_{\text{rel}} \sigma(v_{\text{rel}}) \\ &= n_p^{\text{free}}(T) \left( \frac{\mu}{2\pi k_B T} \right)^{3/2} \int d^3 v_{\text{rel}} e^{-\frac{\mu_{\text{rel}}^2}{2k_B T}} v_{\text{rel}} \sigma(v_{\text{rel}}), \end{aligned} \quad (48)$$

where  $\sigma(v_{\text{rel}})$  is the reaction cross-section calculated at the relative velocity  $v_{\text{rel}}$  of the Be target and the incident proton,  $V_{\text{CM}}$  is the speed of the centre of mass,  $n_p^{\text{free}}(T)$  is the free proton number density at the plasma temperature  $T$ , and  $\mu = \frac{m_p m_{\text{Be}}}{m_p + m_{\text{Be}}}$  is the reduced mass of the two colliding bodies.

The expression for the cross-section of the strong force-driven reaction (5) as a function of the photon temperature in the range  $10 \text{ keV} < k_B T < 100 \text{ keV}$  can be given in atomic units as (Baby et al. 2003; Filipponi et al. 1983a,b; Junghans et al.

2003)

$$\sigma(v_{\text{rel}}) = \frac{1}{e^{2\pi\eta} - 1} \left( \frac{2S_{17}(0)}{\mu v_{\text{rel}}^2} \right), \quad (49)$$

where  $\eta = \frac{Z_p Z_{\text{Be}}}{v_{\text{rel}}}$  is the Sommerfeld parameter,  $Z_p$  and  $Z_{\text{Be}}$  are the atomic numbers of the proton and Be, and  $S_{17}(0) \approx 21.2 \text{ eV b} = 2.7822 \times 10^{-8} \text{ a.u.}$  is the experimental value of the  $S$ -factor, which describes quantum tunnelling through the Coulomb barrier given by the Gamow energy

$$E_G = \frac{(2\pi\alpha Z_p Z_{\text{Be}})^2 \mu c^2}{2} = 13,798.8 \text{ keV.} \quad (50)$$

In Eq. (49), which describes  $s$ -wave scattering of a Coulomb-distorted plane wave on the point-like Be nucleus, we have assumed that the  $S$ -factor has a weak energy dependence, represented by a linear expansion  $S_{17}(E) = S_{17}(0) + S'_{17}E$ , and further that  $S_{17}(E) = S_{17}(0)$  is constant at all energies.

Using the cross-section in Eq. (49) to calculate  $R_{\text{PC}}$  in Eq. (48), the thermally averaged rate per particle pair is therefore

$$R_{\text{PC}} = n_p^{\text{free}}(T) \left( \frac{\mu}{2\pi k_B T} \right)^{\frac{3}{2}} \times \int_0^\infty 4\pi v_{\text{rel}}^2 dv_{\text{rel}} v_{\text{rel}} \frac{1}{e^{2\pi\eta} - 1} \left( \frac{2S_{17}(0)}{\mu v_{\text{rel}}^2} \right) e^{-\frac{\mu v_{\text{rel}}^2}{2k_B T}}. \quad (51)$$

The net number density of free protons,  $n_p^{\text{free}}$ , can be obtained by following the procedure explained in Appendix B.2 (see, in particular, Eq. (B.19)). We note that plasma screening could be taken into account by multiplying the integrand by the Debye static enhancement factor

$$f_{\text{scr}} = \exp\left(\frac{Z_p Z_{\text{Be}} e^2}{\lambda_D k_B T}\right), \quad (52)$$

where  $\lambda_D$  is the Debye radius at the electron density at temperature  $T$ . In addition, a moving proton within the plasma modifies the local electrostatic potential. While it does not alter the Debye length itself, which remains a global collective property of the plasma, it changes the dynamic screening. This can, in turn, modify the local density of positive and negative charges around the beryllium nucleus and thus indirectly affect the Debye length. The results of the PC rate are presented in Tab. (2) for various temperatures below NSE according to Eq. (51). In the last column of Tab. (2), we also show the effect of adding Debye screening to the Coulomb potential barrier that the proton must overcome to be captured by beryllium. This effect is small and only slightly alters the barrier, so it can be safely neglected.

## 6.2. Theory of proton capture with photon emission: quantum approach

The approach described above relies on a classical approximation of two-body scattering. However, the presence of a highly energetic photon background below NSE, further enhanced by the release of  $\gamma$ -radiation upon PC on  ${}^7\text{Be}$ , may generate SE from nuclear excited state levels, increasing the PC cross-section. In principle, this mechanism is similar to laser SE for electrons, where the enhancement of the radiative transition rate is induced by the ambient photon field. The effect is described by a multiplicative factor  $1 + \langle n \rangle$ , where  $\langle n \rangle$  is given by the Bose-Einstein distribution. This enhancement becomes significant at low photon energies and high radiation densities. Here, we aim to include

Table 2: Proton capture rates ( $R_{\text{PC}}$ ) on  ${}^7\text{Be}$  ( $\text{s}^{-1}$ ) as a function of temperature (first column, keV) determined using Eq. (51) (second column), with the addition of nuclear stimulated emission by  $\gamma$  radiation ( $R_{\text{PC+SE}}$ , third column). In the last column we report the Debye screening factor from Eq. (52).

$k_B T$ (keV)	$R_{\text{PC}}$ ( $\text{s}^{-1}$ )	$R_{\text{PC+SE}}$ ( $\text{s}^{-1}$ )	$f_{\text{scr}}$
87.23	1.687e-04	1.701e-04	1.032
54.91	1.034e-05	1.036e-05	1.004
34.57	1.432e-11	1.300e-04	
21.76	1.241e-15	1.136e-04	
13.70	4.872e-17	2.464e-05	
8.623	1.175e-17	5.724e-05	
5.428	2.977e-18	7.181e-14	
3.417	9.238e-19	4.663e-16	
2.151	3.065e-19	2.313e-19	
1.354	9.851e-20	8.533e-20	
0.8723	2.393e-25	2.393e-25	

an analogous mechanism, but involving nuclear rather than electronic SE.

In quantum field theory, each application of the photon creation operator introduces a prefactor when it acts on a single-mode Fock state  $|n\rangle$ , which contains  $n$  photons. This square root factor,  $\sqrt{n+1}$ , increases with the number of photons and can lead to SE. This effect has not been considered previously, and here we aim to estimate its impact on the PC rate.

To account for this effect, we must extend the classical cross-section in Eq. (51) and calculate the differential transition rate for a proton with relative momentum  $\mathbf{p}$  scattered by a Coulomb potential, emitting a photon with momentum  $\mathbf{k}_{\text{ph}}$ , polarisation  $\hat{\epsilon}$ , and energy  $c\mathbf{k}_{\text{ph}}$  as follows:

$$dP_{i \rightarrow f} = 2\pi \left| \langle \psi_{\alpha, \mathbf{p}}^+; n, \hat{\epsilon}, \mathbf{k}_{\text{ph}} | H_{\text{int}} | \psi_{\beta}; n+1, \hat{\epsilon}, \mathbf{k}_{\text{ph}} \rangle \right|^2 \times \delta \left( E_{\alpha} + \frac{p^2}{2\mu} - E_{\beta} - c\mathbf{k}_{\text{ph}} \right) \frac{d^3 \mathbf{k}_{\text{ph}}}{(2\pi)^3}, \quad (53)$$

where  $|\psi_{\alpha, \mathbf{p}}^+; n, \hat{\epsilon}, \mathbf{k}_{\text{ph}}\rangle$  is the tensor product of the quantum state with  $n$  photons,  $|n, \hat{\epsilon}, \mathbf{k}_{\text{ph}}\rangle$ , and the Coulomb-distorted wave function  $|\psi_{\alpha, \mathbf{p}}^+\rangle$  of the system formed by a proton with relative momentum  $\mathbf{p}$  ( $^+$  denotes outgoing wave boundary conditions) impinging on the  ${}^7\text{Be}$  atom in the quantum state denoted by  $\alpha$ , which can be specified, for example, by the quantum numbers  $(n, l, m)$ ;  $\psi_{\beta}$  is the  ${}^8\text{B}$  wave function;  $E_{\alpha}$  and  $E_{\beta}$  are the total energies of the  ${}^7\text{Be}$  and  ${}^8\text{B}$  atoms in the states  $\alpha$  and  $\beta$ , respectively;  $H_{\text{int}} = -i \mathbf{A} \cdot \nabla / \mu$ , where  $\mathbf{A}$  is the photon annihilation operator (or the vector potential of the electromagnetic field) and  $\nabla$  is the gradient (or momentum operator). In this context, we note that

$$(n+1) \left| \langle \psi_{\alpha, \mathbf{p}}^+; 0, \hat{\epsilon}, \mathbf{k}_{\text{ph}} | H_{\text{int}} | \psi_{\beta}; 1, \hat{\epsilon}, \mathbf{k}_{\text{ph}} \rangle \right|^2 = \left| \langle \psi_{\alpha, \mathbf{p}}^+; n, \hat{\epsilon}, \mathbf{k}_{\text{ph}} | H_{\text{int}} | \psi_{\beta}; n+1, \hat{\epsilon}, \mathbf{k}_{\text{ph}} \rangle \right|^2, \quad (54)$$

where the square of the matrix element on the left-hand side corresponds to what is measured in experiments.

To obtain the cross-section without photon background ( $n = 0$  in Eq. (53)), we integrate over all photon directions and polarisations, assuming the long-wavelength limit approximation; that is, the photon wavelength is much larger than the spatial extent of the final proton wave function, which is confined within the

$^8\text{B}$  potential well after capture. This reads per Be atom

$$\begin{aligned}
\sigma_0 &= \frac{1}{\mu p} \int \frac{d^3 k_{\text{ph}}}{(2\pi)^3} \sum_{\hat{\epsilon}} 2\pi \left| \hat{\epsilon} \cdot \langle \psi_{\alpha,p}^+ | \nabla | \psi_{\beta} \rangle \right|^2 \times \\
&\delta \left( E_{\alpha} + \frac{p^2}{2\mu} - E_{\beta} - ck_{\text{ph}} \right) \\
&= \frac{1}{\mu p} \int \frac{k_{\text{ph}}^2 dk_{\text{ph}} d\Omega_{k_{\text{ph}}}}{(2\pi)^3} \sum_{\hat{\epsilon}} 2\pi \left| \hat{\epsilon} \cdot \langle \psi_{\alpha,p}^+ | \nabla | \psi_{\beta} \rangle \right|^2 \times \\
&\delta \left( E_{\alpha} + \frac{p^2}{2\mu} - E_{\beta} - ck_{\text{ph}} \right) \\
&= \frac{1}{\mu p} \int \frac{d\Omega_{k_{\text{ph}}}}{(2\pi)^3} \frac{\left( E_{\alpha} + \frac{p^2}{2\mu} - E_{\beta} \right)^2}{c^3} \sum_{\hat{\epsilon}} 2\pi \left| \hat{\epsilon} \cdot \langle \psi_{\alpha,p}^+ | \nabla | \psi_{\beta} \rangle \right|^2. \tag{55}
\end{aligned}$$

Due to the orthogonality between the photon polarisation vector  $\hat{\epsilon}$  and the wave vector  $k_{\text{ph}}$ , the sum over polarisations can be written as

$$\sum_{\hat{\epsilon}} \left| \hat{\epsilon} \cdot \langle \psi_{\alpha,p}^+ | \nabla | \psi_{\beta} \rangle \right|^2 = \left\| \langle \psi_{\alpha,p}^+ | \nabla | \psi_{\beta} \rangle \right\|^2 - \left| \hat{k}_{\text{ph}} \cdot \langle \psi_{\alpha,p}^+ | \nabla | \psi_{\beta} \rangle \right|^2. \tag{56}$$

Defining  $\theta$  as the angle between  $\hat{k}_{\text{ph}}$  and  $\langle \psi_{\alpha,p}^+ | \nabla | \psi_{\beta} \rangle$ , the expression (56) reduces to

$$\sum_{\hat{\epsilon}} \left| \hat{\epsilon} \cdot \langle \psi_{\alpha,p}^+ | \nabla | \psi_{\beta} \rangle \right|^2 = \left\| \langle \psi_{\alpha,p}^+ | \nabla | \psi_{\beta} \rangle \right\|^2 (1 - \cos^2 \theta). \tag{57}$$

We therefore obtain from Eqs. (55) and (56)

$$\begin{aligned}
\sigma_0 &= \frac{1}{\mu p} \int_0^{\pi} \frac{2\pi \sin \theta d\theta}{(2\pi)^3} \frac{\left( E_{\alpha} + \frac{p^2}{2\mu} - E_{\beta} \right)^2}{c^3} \times \\
&2\pi \left\| \langle \psi_{\alpha,p}^+ | \nabla | \psi_{\beta} \rangle \right\|^2 (1 - \cos^2 \theta) \\
&= \frac{1}{\mu p} \frac{2}{3\pi} \frac{\left( E_{\alpha} + \frac{p^2}{2\mu} - E_{\beta} \right)^2}{c^3} \left\| \langle \psi_{\alpha,p}^+ | \nabla | \psi_{\beta} \rangle \right\|^2. \tag{58}
\end{aligned}$$

Assuming that the squared matrix element can be factorized as a constant coefficient multiplying the Sommerfeld factor, we write

$$\left( E_{\alpha} + \frac{p^2}{2\mu} - E_{\beta} \right)^2 \left\| \langle \psi_{\alpha,p}^+ | \nabla | \psi_{\beta} \rangle \right\|^2 \simeq K \frac{2\pi\eta}{e^{2\pi\eta} - 1}, \tag{59}$$

where  $\eta$  is the Sommerfeld parameter defined previously. This assumption is supported by experimental data (Jungmans et al. 2003; Baby et al. 2003) and is based on the idea that the matrix element on the left is strongly confined within the  $^8\text{B}$  nuclear region due to the capture. Essentially, the proton wave function outside the nucleus before capture may alter the amplitude, but not the shape, of the proton wave function inside after capture, as the latter is mainly determined by the narrow and deep potential well of the nucleus, rather than by its long tail far from the scattering region. Additionally, the kinetic energy outside the nucleus is of the order of keV, while inside the nucleus it is of the order of MeV. The prefactor  $K$  in Eq. (59) essentially contains information about the nucleus, while  $\eta$  incorporates extra-nuclear

information. This factorisation also appears in the phenomenological cross-section in Eq. (49).

The resulting cross-section then reads

$$\sigma_0 \equiv \sigma(\epsilon_p) = \frac{2}{3\pi} \frac{\mu Z_p Z_{\text{Be}}}{\mu p^2} \frac{2\pi}{c^3} \frac{K}{e^{2\pi\eta} - 1} = \frac{S(0)}{\epsilon_p} \frac{1}{e^{2\pi\eta} - 1}, \tag{60}$$

with

$$S(0) = \frac{2Z_p Z_{\text{Be}}}{3\mu c^3} K, \quad \epsilon_p = \frac{p^2}{2\mu}. \tag{61}$$

In atomic units,  $S(0) \simeq 2.7822 \times 10^{-8}$ , giving  $K \simeq 1.1 \times 10^{-5}$ . Finally, the cross-section in the presence of a background of  $n$  photons can be expressed as

$$\sigma_n = (1 + \langle n \rangle) \sigma_0 = \left( 1 + \frac{1}{e^{\epsilon_{\text{ph}}/kT} - 1} \right) \sigma_0, \tag{62}$$

where the average value  $\langle n \rangle$  is calculated by assuming a statisti-

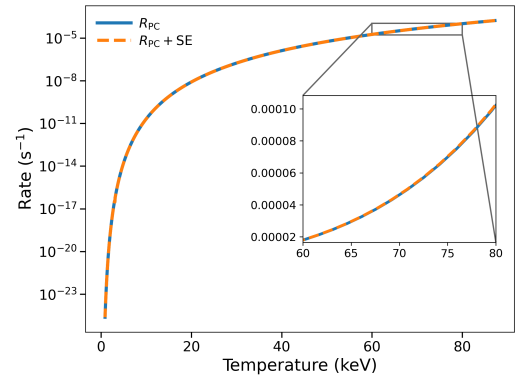


Fig. 5: Proton capture rate on  $^7\text{Be}$  as a function of temperature. The solid line shows  $R_{\text{PC}}$ , while the dashed line shows  $R_{\text{PC}} + \text{SE}$ , where SE denotes stimulated emission. The inset zooms into the 60–80 keV range (box in the main panel).

cal mixture of photons distributed according to Bose-Einstein statistics at an energy corresponding to the photon emission, which of course depends on the initial kinetic energy of the proton. The results for the PC rate with SE are presented in the third column of Tab. (2) for various temperatures below NSE. As the temperature decreases, the effect of SE disappears due to the absence of the photon background at low temperatures. Under these conditions the rates with SE (third column in Tab. (2)) and without SE (second column in Tab. (2)) become similar. These data are also shown in Fig. (5).

### 6.3. Theory of proton capture with energy transfer to a continuum electron (Auger-like process)

Finally, we have studied a different PC process in which an excited  $^8\text{B}$  nucleus, after PC on  $^7\text{Be}$ , decays by emitting a virtual  $\gamma$ -photon that transfers energy to a nearby continuum electron (see Eq. (6)). This is a three-body process, similar to an Auger process, which typically occurs in atoms, molecules, and solids with an inner-shell vacancy that de-excites by ejecting valence electrons from bound levels with characteristic energies, appearing as peaks in the energy spectrum (Taioli et al. 2010; Taioli & Simonucci 2021; Taioli & Dapor 2025).

Typically, non-radiative Auger decay competes with radiative decay, that is, the emission of photons, depending on factors such as atomic number and ionisation state. In BBN conditions, however, the  $^7\text{Be}$  nucleus is usually fully ionised and surrounded by a plasma of free protons and electrons. Auger conversion under these conditions may differ from the bound-to-continuum emission process described above and may instead be a continuum-to-continuum mechanism, in which a virtual photon emitted by the excited nucleus scatters a continuum electron and changes its momentum. Our aim is to determine whether this non-radiative Auger conversion channel could compete with the radiative PC process studied in the previous section.

The differential transition rate for the Auger-like capture process, in atomic units, is

$$dP_{i \rightarrow f} = 2\pi \left| \langle \psi_{\alpha,p}^+; \varphi_k | H_{int} | \psi_\beta; \varphi_{k'} \rangle \right|^2 \times \delta \left( E_\alpha + \frac{p^2}{2\mu} + c \sqrt{k^2 + c^2} - E_\beta - c \sqrt{k'^2 + c^2} \right) \frac{d^3 k}{(2\pi)^3} \frac{d^3 k'}{(2\pi)^3}, \quad (63)$$

where  $H_{int} = 1/|\mathbf{r}_p - \mathbf{r}_e|$  is the Coulomb potential describing the interaction between an electron at position  $\mathbf{r}_e$  and a proton at  $\mathbf{r}_p$ , connecting the initial state ( $|\psi_{\alpha,p}^+; \varphi_k\rangle$ ) and the final state ( $|\psi_\beta; \varphi_{k'}\rangle$ ), in which an electron  $\varphi_k$  with momentum  $\mathbf{k}$  in the energy continuum is scattered out with momentum  $\mathbf{k}'$  upon absorption of a virtual  $\gamma$ -photon produced by the nuclear transition from state  $\alpha$  to state  $\beta$  induced by capture of a proton with momentum  $\mathbf{p}$ . This transition rate must be averaged over all initial electron states and integrated over all final states to obtain the corresponding cross-section per Be atom as follows:

$$\sigma = \frac{\mu}{p} \int \int 2\pi \frac{d^3 k}{(2\pi)^3} \frac{d^3 k'}{(2\pi)^3} \left| \langle \psi_{\alpha,p}^+; \varphi_k | H_{int} | \psi_\beta; \varphi_{k'} \rangle \right|^2 \times \delta \left( E_\alpha + \frac{p^2}{2\mu} + c \sqrt{k^2 + c^2} - E_\beta - c \sqrt{k'^2 + c^2} \right) \rho(\mathbf{k}), \quad (64)$$

where  $\rho(\mathbf{k})$  is the electron density at momentum  $\mathbf{k}$ . Approximating electron wave functions by plane waves near the  $^7\text{Be}$  nucleus ( $\mathbf{r}_e \approx \mathbf{r}_p$ )

$$\sigma = \frac{\mu}{p} \int \int 2\pi \frac{d^3 k}{(2\pi)^3} \frac{d^3 k'}{(2\pi)^3} \left| \langle \psi_{\alpha,p}^+ | e^{i(\mathbf{k}-\mathbf{k}') \cdot \mathbf{r}_p} | \psi_\beta \rangle \right|^2 \times \frac{(4\pi)^2 \rho(\mathbf{k})}{|\mathbf{k}' - \mathbf{k}|^4} \delta \left( E_\alpha + \frac{p^2}{2\mu} + c \sqrt{k^2 + c^2} - E_\beta - c \sqrt{k'^2 + c^2} \right). \quad (65)$$

Assuming orthogonality of  $\psi_{\alpha,p}^+$  and  $\psi_\beta$ , and expanding the exponential for small arguments within the nuclear volume ( $|e^{i(\mathbf{k}-\mathbf{k}') \cdot \mathbf{r}_p}| \sim |(\mathbf{k} - \mathbf{k}') \cdot \mathbf{r}_p|$ ), we obtain

$$\sigma \simeq \frac{\mu}{p} \int \int 2\pi \frac{d^3 k}{(2\pi)^3} \frac{d^3 k'}{(2\pi)^3} \left| (\mathbf{k} - \mathbf{k}') \cdot \langle \psi_{\alpha,p}^+ | \mathbf{r}_p | \psi_\beta \rangle \right|^2 \times \frac{(4\pi)^2 \rho(\mathbf{k})}{|\mathbf{k}' - \mathbf{k}|^4} \delta \left( E_\alpha + \frac{p^2}{2\mu} + c \sqrt{k^2 + c^2} - E_\beta - c \sqrt{k'^2 + c^2} \right). \quad (66)$$

Integrating over  $d\mathbf{k}'$ , we obtain

$$\bar{k}^2 = \left( \frac{E_\alpha - E_\beta + \frac{p^2}{2\mu}}{c} + \sqrt{k^2 + c^2} \right)^2 - c^2, \quad (67)$$

which leads to

$$\sigma \simeq \frac{\mu}{p} \int \int \frac{2\pi (4\pi)^2}{(2\pi)^6} \times \frac{\left| (\mathbf{k} - \bar{k}\hat{\mathbf{k}}) \cdot \langle \psi_{\alpha,p}^+ | \mathbf{r}_p | \psi_\beta \rangle \right|^2}{|\mathbf{k}' - \mathbf{k}|^4} \rho(\mathbf{k}) k^2 \bar{k}^2 dk d\Omega_{\hat{\mathbf{k}}} d\Omega_{\hat{\mathbf{k}}'}. \quad (68)$$

We further assume that  $\rho(\mathbf{k}) = \rho(k)$  and integrate over the differential solid angle  $d\Omega_{\hat{\mathbf{k}}'} = \sin \theta' d\theta' d\phi'$ , where the unit vector  $\hat{\mathbf{k}}'$  spans the unit sphere and points in the direction specified by the angular coordinates  $(\theta', \phi')$ . The  $z$ -axis is aligned with the direction of  $\hat{\mathbf{k}}$ , and the  $xz$ -plane contains both  $\hat{\mathbf{k}}$  and  $\langle \psi_{\alpha,p}^+ | \mathbf{r}_p | \psi_\beta \rangle$ . If  $\theta$  is the angle between  $\hat{\mathbf{k}}$  and  $\langle \psi_{\alpha,p}^+ | \mathbf{r}_p | \psi_\beta \rangle$ , and  $\theta'$  is the angle between  $\hat{\mathbf{k}}$  and  $\hat{\mathbf{k}}'$ , then  $\hat{\mathbf{k}} \cdot \langle \psi_{\alpha,p}^+ | \mathbf{r}_p | \psi_\beta \rangle = \left| \langle \psi_{\alpha,p}^+ | \mathbf{r}_p | \psi_\beta \rangle \right| \cos \theta$  and  $\hat{\mathbf{k}} \cdot \hat{\mathbf{k}}' = \cos \theta'$  while  $\hat{\mathbf{k}}' \cdot \langle \psi_{\alpha,p}^+ | \mathbf{r}_p | \psi_\beta \rangle = \left| \langle \psi_{\alpha,p}^+ | \mathbf{r}_p | \psi_\beta \rangle \right| (\sin \theta \sin \theta' \cos \phi' + \cos \theta \cos \theta')$ . Then Eq. (68) reads:

$$\sigma \simeq \frac{\mu}{p} \int_0^\infty dk \int_0^\pi \sin \theta d\theta \int_0^{2\pi} d\phi \int_0^\pi \sin \theta' d\theta' \int_0^{2\pi} d\phi' \frac{2\pi (4\pi)^2}{(2\pi)^6} \times \frac{\left| k \cos \theta - \bar{k} (\sin \theta \sin \theta' \cos \phi' + \cos \theta \cos \theta') \right|^2}{|k^2 + \bar{k}^2 - 2k\bar{k} \cos \theta'|^2} \times \left| \langle \psi_{\alpha,p}^+ | \mathbf{r}_p | \psi_\beta \rangle \right|^2 \rho(k) k^2 \bar{k}^2 dk d\Omega_{\hat{\mathbf{k}}}, \quad (69)$$

which, when integrated over  $d\phi'$ , leads to

$$\sigma \simeq \frac{\mu}{p} \int_0^\infty dk \int_0^\pi \sin \theta d\theta \int_0^{2\pi} d\phi \int_0^\pi \sin \theta' d\theta' \frac{64\pi^4}{(2\pi)^6} \times \frac{\left| k^2 \cos^2 \theta - 2k\bar{k} \cos^2 \theta \cos \theta' + \frac{1}{2} \bar{k}^2 \sin^2 \theta \sin^2 \theta' + \bar{k}^2 \cos^2 \theta \cos^2 \theta' \right|}{|k^2 + \bar{k}^2 - 2k\bar{k} \cos \theta'|^2} \times \left| \langle \psi_{\alpha,p}^+ | \mathbf{r}_p | \psi_\beta \rangle \right|^2 \rho(k) k^2 \bar{k}^2 dk d\Omega_{\hat{\mathbf{k}}}. \quad (70)$$

Let us integrate over  $\hat{\mathbf{k}}$  (or over the variables  $\phi$  and  $\theta$ ). Observing that the integrand does not depend on  $\phi$ , we obtain

$$\begin{aligned} \sigma &\simeq \frac{\mu}{p} \int_0^\infty dk \int_0^\pi \frac{128\pi^5}{(2\pi)^6} \sin \theta' d\theta' \times \\ &\int_0^\pi \frac{\left| k^2 \cos^2 \theta - 2k\bar{k} \cos^2 \theta \cos \theta' + \frac{1}{2} \bar{k}^2 \sin^2 \theta \sin^2 \theta' + \bar{k}^2 \cos^2 \theta \cos^2 \theta' \right|}{|k^2 + \bar{k}^2 - 2k\bar{k} \cos \theta'|^2} \sin \theta d\theta \times \\ &\left| \langle \psi_{\alpha,p}^+ | \mathbf{r}_p | \psi_\beta \rangle \right|^2 \rho(k) k^2 \bar{k}^2 \\ &= \frac{\mu}{p} \int_0^\infty dk \int_0^\pi \frac{128\pi^5}{(2\pi)^6} \sin \theta' d\theta' \left| \langle \psi_{\alpha,p}^+ | \mathbf{r}_p | \psi_\beta \rangle \right|^2 \times \\ &\int_0^\pi \frac{\left| \frac{1}{3} k^2 - \frac{4}{3} k\bar{k} \cos \theta' + \frac{2}{3} \bar{k}^2 \sin^2 \theta' + \frac{2}{3} \bar{k}^2 \cos^2 \theta' \right|}{|k^2 + \bar{k}^2 - 2k\bar{k} \cos \theta'|^2} \rho(k) k^2 \bar{k}^2 \\ &= \frac{\mu}{p} \int_0^\infty dk \int_0^\pi \frac{4}{3\pi} \frac{\left| \langle \psi_{\alpha,p}^+ | \mathbf{r}_p | \psi_\beta \rangle \right|^2}{|k^2 + \bar{k}^2 - 2k\bar{k} \cos \theta'|} \sin \theta' d\theta' \rho(k) k^2 \bar{k}^2 \\ &= \frac{\mu}{p} \int_0^\infty dk \log \left( \frac{|k^2 + \bar{k}^2 + 2k\bar{k}|}{|k^2 + \bar{k}^2 - 2k\bar{k}|} \right) \rho(k) \frac{k^2 \bar{k}^2}{2k\bar{k}}. \end{aligned} \quad (71)$$

Finally, using Eq. (59) we obtain

$$\begin{aligned} \sigma &\simeq \frac{1}{\mu p} \frac{2K}{3\pi \left( E_\alpha + \frac{p^2}{2\mu} - E_\beta \right)^4} \frac{2\pi\eta}{e^{2\pi\eta} - 1} \times \\ &\int_0^\infty dk \log \left( \frac{|k^2 + \bar{k}^2 + 2k\bar{k}|}{|k^2 + \bar{k}^2 - 2k\bar{k}|} \right) \rho(k) k\bar{k}, \end{aligned} \quad (72)$$

where the electron density is  $\rho(k) = \frac{2}{e^{\frac{c\sqrt{k^2 + e^2 - \mu}}{k_B T}} + 1}$ , and one can use  $K$  from Eq. (61). We emphasise that in Eq. (72), a different initial proton kinetic energy ( $p^2/2m$ ) results in a different virtual photon energy and, consequently, a different momentum of the scattered electron in the continuum,  $\bar{k}$ , which leads to a different available phase space. Using Eq. (72) for proton kinetic energies of 10, 30, 60, and 100 keV, and a plasma temperature in the range  $1 < k_B T < 100$  keV to determine the electron density at the nucleus, the resulting cross-sections as a function of incident proton energy are reported in Tab. (3). These results are

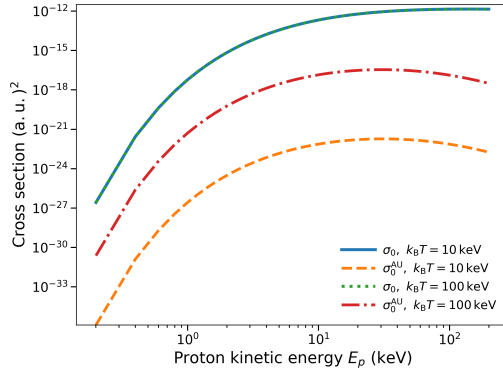


Fig. 6: Proton capture cross-sections on  ${}^7\text{Be}$  as a function of proton kinetic energy,  $E_p$ . The solid and dashed curves show the cross-sections without ( $\sigma_0$ ) and with ( $\sigma_0^{\text{AU}}$ ) the Auger mechanism at  $k_B T = 10$  keV, respectively. The dotted and dash-dotted curves show the corresponding cross-sections at  $k_B T = 100$  keV. Cross-sections are given in units of (a.u.)<sup>2</sup>.

also shown in Fig. (6).

In particular, we note that at a plasma temperature of  $k_B T = 100$  keV ( $n_e = 240 \text{ a}_0^{-3}$ ), for a 2 keV kinetic energy of the protonic projectile, the contribution of the three-body Auger-type transition is approximately  $10^{-4}\%$  of the radiative PC cross-section. In contrast, at  $k_B T = 10$  keV ( $n_e = 2.64 \times 10^{-9} \text{ a}_0^{-3}$ ), for a proton with 80 keV kinetic energy, the Auger contribution is only about  $\approx 10^{-10}\%$  of the radiative PC cross-section. The Auger-like mechanism does not significantly contribute to the total PC cross-section at temperatures much below NSE, as the electron density near the nucleus is typically low, while its relative importance increases at higher temperatures and proton kinetic energy.

## 7. Discussion and conclusions

In this work, we have reassessed several weak and radiative processes involving  ${}^7\text{Be}$  and  ${}^7\text{Li}$  under Big Bang Nucleosynthesis (BBN) conditions, aiming to quantify their possible impact on the long-standing cosmological lithium problem. In particular, we have focused on (i) EC and AC on  ${}^7\text{Be}$ ; (ii) positron emission from the nuclear excited state of  ${}^7\text{Be}$ ; and (iii) PC via both the standard radiative channel  ${}^7\text{Be}(p, \gamma){}^8\text{B}$ , including the possibility of stimulated emission from the dense photon background, and an Auger-like three-body variant, in which the capture energy is transferred to a continuum electron.

Our calculations were performed within a first-principles framework that treats leptonic and hadronic currents consistently and includes temperature- and density-dependent effects appropriate to the post-NSE epoch ( $10 \text{ keV} < k_B T < 100 \text{ keV}$ ). In contrast to previous estimates based on semi-empirical  $\log(f)$

systematics, our approach explicitly accounts for ionisation, excitation, relativistic effects, and the actual populations of bound and continuum leptonic states in the primordial plasma, and calculates the nuclear wave functions of ground and excited states within our ab initio framework.

We find that the in-situ EC rate of  ${}^7\text{Be}$  decreases rapidly as the Universe expands and cools, reflecting the dilution of the electron density and the progressive departure from pair equilibrium. The inclusion of the AC channel enhances the total weak interaction rate at early times; however, its contribution becomes negligible as the neutrino background dilutes after weak freeze-out. Overall, the combined effect of EC and AC, and  $\beta^+$ -decay leads to significant corrections to the  ${}^7\text{Be}$  destruction channels during BBN, resulting in a half-life of approximately 1.5 days. However, this is still not entirely sufficient to reconcile the observations with the BBN model in the very early stages of the Universe.

For PC, we confirm that plasma screening leads to only a modest enhancement (at the level of a few percent) of the thermally averaged  ${}^7\text{Be}(p, \gamma){}^8\text{B}$  rate in the temperature range considered. The Auger-like three-body capture mechanism, although conceptually interesting and analogous to internal conversion processes in atomic physics, is found to be subdominant. At  $k_B T \approx 100$  keV, its cross-section is approximately 0.004% of the radiative PC of the radiative-only channel, but it decreases steeply with temperature and becomes negligible ( $\sim 10^{-10}$  of the radiative rate) by  $k_B T \approx 10$  keV. As a result, this channel does not provide a significant additional pathway for  ${}^7\text{Be}$  depletion during the relevant BBN epoch. This picture does not change significantly if we also consider adding a novel mechanism to the standard PC mechanism, due to the presence of a high-density  $\gamma$ -photon background, which is conceptually similar to stimulated emission caused by lasers in cavities. The enhancement of the cross-section due to this background is less than 5%.

Taken together, our results indicate that neither enhanced weak interaction rates nor Auger-like PC processes are capable, on their own, of resolving the discrepancy between the primordial  ${}^7\text{Li}$  abundance predicted by standard BBN and that inferred from observations of metal-poor halo stars.

Nevertheless, our study highlights the importance of computing nuclear and electroweak reaction rates under cosmological conditions using accurate first-principles simulations before considering unexplored BSM physics. Future work should refine the three-body matrix element beyond the plane-wave approximation, reassess screening using kinetic plasma models, and propagate the updated rates through a complete BBN network. Moreover, we believe the conditions under which BBN models predict nucleus formation should be revised to account for possible earlier formation, even before nuclear statistical equilibrium, under conditions different from those typically considered. This would further reduce the decay half-life of the relevant isotopes, resulting in closer agreement with observations.

*Acknowledgements.* This work has received funding from the European Union under the Mimosa grant agreement No. 10104665 and from INFN through the project PANDORA Gr3, funded by the 3rd National Scientific Commission. The authors acknowledge fruitful discussions with Dr. Martino Silvetti (University of Modena and Reggio Emilia).

Table 3: Proton capture cross-sections on  ${}^7\text{Be}$  as a function of the incoming proton kinetic energy (first column,  $E_p$  in keV).  $\sigma_0$  denotes the cross-section without the Auger-like interaction.  $\sigma_0^{\text{AU}}$  denotes the cross-section including the Auger-like mechanism. Cross-sections are given in (a.u.)<sup>2</sup>.

$k_B T = 10 \text{ (keV)}$			$30 \text{ (keV)}$			$60 \text{ (keV)}$			$100 \text{ (keV)}$		
$E_p \text{ (keV)}$	$\sigma_0$	$\sigma_0^{\text{AU}}$	$\sigma_0$	$\sigma_0^{\text{AU}}$	$\sigma_0$	$\sigma_0$	$\sigma_0^{\text{AU}}$	$\sigma_0$	$\sigma_0$	$\sigma_0^{\text{AU}}$	
2	$6.84 \times 10^{-16}$	$3.03 \times 10^{-25}$	$6.84 \times 10^{-16}$	$3.24 \times 10^{-25}$	$6.84 \times 10^{-16}$	$7.39 \times 10^{-22}$	$6.84 \times 10^{-16}$	$5.79 \times 10^{-20}$	$6.84 \times 10^{-16}$	$5.79 \times 10^{-20}$	
20	$5.87 \times 10^{-13}$	$1.60 \times 10^{-22}$	$5.87 \times 10^{-13}$	$1.70 \times 10^{-22}$	$5.87 \times 10^{-13}$	$3.86 \times 10^{-19}$	$5.87 \times 10^{-13}$	$3.01 \times 10^{-17}$	$5.87 \times 10^{-13}$	$3.01 \times 10^{-17}$	
40	$1.04 \times 10^{-12}$	$1.75 \times 10^{-22}$	$1.04 \times 10^{-12}$	$1.85 \times 10^{-22}$	$1.04 \times 10^{-12}$	$4.18 \times 10^{-19}$	$1.04 \times 10^{-12}$	$3.25 \times 10^{-17}$	$1.04 \times 10^{-12}$	$3.25 \times 10^{-17}$	
80	$1.33 \times 10^{-12}$	$9.93 \times 10^{-23}$	$1.33 \times 10^{-12}$	$1.05 \times 10^{-22}$	$1.33 \times 10^{-12}$	$2.34 \times 10^{-19}$	$1.33 \times 10^{-12}$	$1.81 \times 10^{-17}$	$1.33 \times 10^{-12}$	$1.81 \times 10^{-17}$	
100	$1.38 \times 10^{-12}$	$7.22 \times 10^{-23}$	$1.38 \times 10^{-12}$	$7.58 \times 10^{-23}$	$1.38 \times 10^{-12}$	$1.69 \times 10^{-19}$	$1.38 \times 10^{-12}$	$1.30 \times 10^{-17}$	$1.38 \times 10^{-12}$	$1.30 \times 10^{-17}$	
140	$1.40 \times 10^{-12}$	$3.93 \times 10^{-23}$	$1.40 \times 10^{-12}$	$4.11 \times 10^{-23}$	$1.40 \times 10^{-12}$	$9.13 \times 10^{-20}$	$1.40 \times 10^{-12}$	$6.99 \times 10^{-18}$	$1.40 \times 10^{-12}$	$6.99 \times 10^{-18}$	
160	$1.40 \times 10^{-12}$	$2.96 \times 10^{-23}$	$1.40 \times 10^{-12}$	$3.09 \times 10^{-23}$	$1.40 \times 10^{-12}$	$6.86 \times 10^{-20}$	$1.40 \times 10^{-12}$	$5.24 \times 10^{-18}$	$1.40 \times 10^{-12}$	$5.24 \times 10^{-18}$	
180	$1.39 \times 10^{-12}$	$2.27 \times 10^{-23}$	$1.39 \times 10^{-12}$	$2.36 \times 10^{-23}$	$1.39 \times 10^{-12}$	$5.23 \times 10^{-20}$	$1.39 \times 10^{-12}$	$3.99 \times 10^{-18}$	$1.39 \times 10^{-12}$	$3.99 \times 10^{-18}$	
200	$1.38 \times 10^{-12}$	$1.76 \times 10^{-23}$	$1.38 \times 10^{-12}$	$1.83 \times 10^{-23}$	$1.38 \times 10^{-12}$	$4.04 \times 10^{-20}$	$1.38 \times 10^{-12}$	$3.08 \times 10^{-18}$	$1.38 \times 10^{-12}$	$3.08 \times 10^{-18}$	

## References

- Adelberger, E. G., García, A., Robertson, R. H., et al. 2011, *Reviews of Modern Physics*, 83, 195
- Agodi, C., Cappuzzello, F., Cardella, G., et al. 2023, *The European Physical Journal Plus*, 138, 1038
- Andrews, A., Rodono, M., Linsky, J., et al. 1988, *Astronomy and Astrophysics* (ISSN 0004-6361), vol. 204, no. 1-2, Oct. 1988, p. 177-192. MPI-CNR-supported research., 204, 177
- Asplund, M., Grevesse, N., Sauval, A. J., & Scott, P. 2009, *Annual review of astronomy and astrophysics*, 47, 481
- Baby, L. T., Bordeanu, C., Goldring, G., et al. 2003, *Phys. Rev. C*, 67, 065805
- Bahcall, J. N. 1961, *Phys. Rev.*, 124, 495
- Bahcall, J. N. 1962, *Physical Review*, 126, 1143
- Bahcall, J. N. & Moeller, C. P. 2018, in *Solar Neutrinos* (CRC Press), 222-222
- Balachandran, S. 1995, *Astrophysical Journal* v. 446, p. 203, 446, 203
- Bertulani, C., Mukhamedzhanov, A., et al. 2018, in *EPJ Web of Conferences*, Vol. 184, EDP Sciences, 01002
- Boesgaard, A. M. & Tripicco, M. J. 1986a, *Astrophysical Journal*, Part 1 (ISSN 0004-637X), vol. 303, April 15, 1986, p. 724-739., 303, 724
- Boesgaard, A. M. & Tripicco, M. J. 1986b, *Astrophysical Journal*, Part 2-Letters to the Editor (ISSN 0004-637X), vol. 302, March 15, 1986, p. L49-L53., 302, L49
- Bonifacio, P. et al. 2007, *Astronomy & Astrophysics*, 462, 851
- Cameron, R. P. 2022, *Physica Scripta*, 97, 035502
- Caprini, C. & Ferreira, P. G. 2005, *JCAP*, 02, 006, arXiv:hep-ph/0310066
- Casuso, E. & Beckman, J. E. 2003, *Publications of the Astronomical Society of Japan*, 55, 247
- Charbonnel, C. & Lagarde, N. 2010, *Astronomy & Astrophysics*, 522, A10
- Coc, A. & Vangioni, E. 2017, *International Journal of Modern Physics E*, 26, 1741002
- Cyburt, R. H., Fields, B. D., Olive, K. A., & Yeh, T.-H. 2016, *Rev. Mod. Phys.*, 88, 015004
- Damone, L., Barbagallo, M., Mastromarco, M., et al. 2018, *Physical review letters*, 121, 042701
- Dolgov, A. D. 2002, *Physics Reports*, 370, 333
- Eggenberger, P., Meynet, G., Maeder, A., et al. 2010, *Astronomy & Astrophysics*, 519, A116
- Fields, B., Molaro, P., & Sarkar, S. 2014, *Chinese Physics C*, 38, 339
- Fields, B. D. 2011, *Annual Review of Nuclear and Particle Science*, 61, 47
- Fields, B. D. & Olive, K. A. 2022, *Journal of Cosmology and Astroparticle Physics*, 2022, 078
- Filippone, B. W., Elwyn, A. J., Davids, C. N., & Koetke, D. D. 1983a, *Phys. Rev. Lett.*, 50, 412
- Filippone, B. W., Elwyn, A. J., Davids, C. N., & Koetke, D. D. 1983b, *Phys. Rev. C*, 28, 2222
- Fuller, G. M., Fowler, W. A., & Newman, M. J. 1982, *Astrophysical Journal Supplement Series*, 48, 279
- Fuller, G. M. & Smith, C. J. 2010, *Phys. Rev. D*, 82, 125017
- Iben Jr, I., Kalata, K., & Schwartz, J. 1967, *Astrophysical Journal*, vol. 150, p. 1001, 150, 1001
- Junghans, A. R., Mohrman, E. C., Snover, K. A., et al. 2003, *Phys. Rev. C*, 68, 065803
- Litvinov, Y. A. & Bosch, F. 2010, *Reports on Progress in Physics*, 74, 016301
- Mascali, D., Santonocito, D., Amaducci, S., et al. 2022, *Universe*, 8, 80
- Mascali, D., Santonocito, D., Busso, M., et al. 2023, in *EPJ Web of Conferences*, Vol. 279, EDP Sciences, 06007
- Michaud, G. 1986, *Astrophysical Journal*, Part 1 (ISSN 0004-637X), vol. 302, March 15, 1986, p. 650-655., 302, 650
- Michaud, G. & Charbonneau, P. 1991, *Space Science Reviews*, 57, 1
- Miranda, Oswaldo D. 2025, *A&A*, 701, A164
- Mishra, B., Pidatella, A., Taioli, S., Simonucci, S., & Mascali, D. 2024, arXiv preprint arXiv:2407.01787
- Moresi, T., Taioli, S., & Simonucci, S. 2018, *Advanced Theory and Simulations*, 1, 1800086
- Mukhanov, V. 2005, *Physical Foundations of Cosmology* (Cambridge University Press)
- National Nuclear Data Center. 2023, NuDat 3.0: Nuclear Structure and Decay Data, <https://www.nndc.bnl.gov/nudat3/>, accessed: 2025-09-22
- Palmerini, S., Busso, M., Simonucci, S., & Taioli, S. 2016, *Journal of Physics: Conference Series*, 665, 012014
- Perkins, D. 2009, *Particle Astrophysics*, Oxford Master Series in Particle Physics, Astrophysics, and Cosmology (Oxford University Press)
- Pitrou, C., Coc, A., Uzan, J.-P., & Vangioni, E. 2018, *Phys. Rept.*, 754, 1
- Planck Collaboration, Aghanim, N., Akrami, Y., et al. 2020, *A&A*, 641, A5
- Richard, O., Michaud, G., & Richer, J. 2005, *The Astrophysical Journal*, 619, 538
- Schwierz, N., Wiedenhöver, I., & Volya, A. 2007, arXiv: Nuclear Theory
- Simonucci, S., Taioli, S., Palmerini, S., & Busso, M. 2013, *The Astrophysical Journal*, 764, 118
- Sivarani, T., Bonifacio, P., Molaro, P., et al. 2004, *Astronomy & Astrophysics*, 413, 1073
- Spite, M. & Spite, F. 2012, *Astronomy & Astrophysics*, 541, A143
- Taioli, S. & Dapor, M. 2025, *Surface Science Reports*, 80, 100646
- Taioli, S. & Simonucci, S. 2021, *Annual Reports in Computational Chemistry*, 17
- Taioli, S., Simonucci, S., Calliari, L., & Dapor, M. 2010, *Physics reports*, 493, 237
- Taioli, S., Vescovi, D., Busso, M., et al. 2022, *The Astrophysical Journal*, 933, 158
- Takahashi, K., Boyd, R. N., Mathews, G. J., & Yokoi, K. 1987, *Phys. Rev. C*, 36, 1522
- Takahashi, K. & Yokoi, K. 1983, *Nuclear Physics A*, 404, 578
- Takahashi, K. & Yokoi, K. 1987, *Atomic Data and Nuclear Data Tables*, 36, 375
- Vescovi, D., Piersanti, L., Cristallo, S., et al. 2019, *Astronomy & Astrophysics*, 623, 7
- Weinberg, S. 2008a, *Cosmology* (Oxford University Press)
- Weinberg, S. 2008b, *Cosmology* (Oxford, UK: Oxford University Press)
- Yu, H., Yang, K., & Li, J. 2022, *European Physical Journal C*, 82, 328

## Appendix A: Numerical solution of the radial Dirac equation

The time-independent Dirac equation (32) in radial coordinates, due to the spherically symmetric internuclear and interelectronic interaction potentials, can be written as

$$\frac{d\psi}{dr} = F_E(\psi, r), \quad (\text{A.1})$$

where  $\psi = (u, d)^T$  is the four-component Dirac spinor and  $F_E$  is a linear operator in both  $\psi$  and the eigenvalue  $E$ . Equation (A.1) is a first order differential equation, which we solve on a real-space grid of points. Although the DHF equations include a non-local Fock term, they remain linear in  $\psi$ . Furthermore, in our method, we use an LDA approximation for the many-electron interaction (see Eq. (37)).

To solve the differential Eq. (A.1) we employ a collocation method, a variant of the Runge–Kutta approach (Morresi et al. 2018). The radial interval  $[0, R_{\max}]$  (where  $R_{\max}$  depends on whether the orbital is bound or continuum) is divided into grid points  $0 = r_0 < \dots < r_N = R_{\max}$ , chosen by Gauss–Legendre sampling so that the same weights can be used for nuclear-volume integrals.

Bound states are computed with  $R_{\max} \simeq 25$  a.u., whereas continuum states require  $R_{\max} \simeq 100$  a.u.

Each subinterval  $[r_{j-1}, r_j]$  contains  $s_j$  collocation points  $x_{j,l}$ , where the derivative appearing in Eq. (A.1) is approximated as

$$\frac{d\psi}{dr} \approx \sum_{l=1}^{s_j} q_{j,l} \phi'_{j,l}(r), \quad (\text{A.2})$$

with  $\phi_{j,l}$  chosen such that  $\phi'_{j,l}(x_{j,m}) = \delta_{lm}$ . Defining

$$a_{j,lm} = \int_{r_{j-1}}^{x_{j,l}} \phi'_{j,m}(x) dx, \quad b_{j,l} = \int_{r_{j-1}}^{r_j} \phi'_{j,l}(x) dx, \quad (\text{A.3})$$

the Dirac equation reduces to the block-triangular eigenvalue problem (Morresi et al. 2018)

$$[c\gamma + (V + \gamma_0 mc^2)A - EA]q = 0, \quad (\text{A.4})$$

where  $q$  collects all coefficients  $q_{j,l}$ ,  $A$  is the sparse matrix containing the  $a_{j,lm}$  and  $b_{j,l}$ , and  $\gamma$  is  $2 \times 2$  matrix. A unitary transformation  $A \rightarrow AQ$  further reduces the bandwidth, enabling efficient eigenvalue extraction using an *LDU* decomposition.

The wave function follows from  $\psi(r) = Aq$ , and for continuum solutions the normalization is fixed at the outer boundary using the asymptotic Coulomb functions,

$$u \sim \frac{\sqrt{\epsilon + c^2}}{\sqrt{\pi p}} \cos(pr + \delta), \quad v \sim -\frac{\sqrt{\epsilon - c^2}}{\sqrt{\pi p}} \sin(pr + \delta), \quad (\text{A.5})$$

with  $\epsilon = \sqrt{p^2 c^2 + c^4}$  and  $\delta$  as the phase shift due to the atomic Coulomb potential (Morresi et al. 2018). Because the normalization oscillates with  $R_{\max}$ , we average it over one full oscillation period of the continuum wave function. More details on computational methods are given in Ref. (Morresi et al. 2018).

## Appendix B: Particle densities and their chemical potentials

To calculate EC and PC rates, including stimulated emission, we need to determine the densities of the particles involved in the reactions. Below, we derive the analytical relation for calculating the densities of photons, electrons, positrons, neutrinos, neutrons, protons, and their respective antiparticles.

### B.1. Photon density

Since the photon mass is 0, its energy  $E$  and momentum  $p$  are related by the dispersion relation  $E = pc$ . The number of photons in an infinitesimal volume of phase space  $d^3q d^3p$ , where  $q$  is the position, is

$$dn_\gamma = \frac{d^3q d^3p}{h^3} \frac{g}{e^{\beta E} - 1}, \quad (\text{B.1})$$

where  $\beta = \frac{1}{k_B T_\gamma}$ ,  $h$  is the Planck constant, and  $g$  is the degeneracy number for photons. Photons are spin-1 particles and are characterised by two independent polarisations; therefore, for photons,  $g = 2$ . The factor  $\frac{1}{e^{\beta E} - 1}$  ensures that photons are distributed according to Bose–Einstein statistics. If we divide expression (B.1) by  $d^3q$ , we obtain

$$dn_\gamma(p) = \frac{d^3p}{h^3} \frac{g}{e^{\beta E} - 1} = \frac{4\pi p^2 dp}{8\pi^3 \hbar^3} \frac{g}{e^{\beta E} - 1} = \frac{g}{2\pi^2 \hbar^3} \frac{p^2 dp}{e^{\beta E} - 1}, \quad (\text{B.2})$$

which is the infinitesimal volumetric variation of the photon density for momentum ranging from  $p$  to  $p + dp$  and  $\hbar = h/2\pi$  is the reduced Planck constant. From  $E = pc$ , it follows that  $dE = c dp$ , and

$$dn_\gamma(E) = \frac{g}{2\pi^2 \hbar^3 c^3} k_B^3 T_\gamma^3 \frac{\beta^3 E^2 dE}{e^{\beta E} - 1}. \quad (\text{B.3})$$

The infinitesimal variation of the photon energy per unit volume is

$$du_\gamma = Edn_\gamma(E) = \frac{g}{2\pi^2 \hbar^3 c^3} k_B^4 T_\gamma^4 \frac{\beta^4 E^3 dE}{e^{\beta E} - 1}. \quad (\text{B.4})$$

The total photon density and energy density are obtained by integrating the Eqs. (B.3) and (B.4):

$$n_\gamma(T) = \frac{g}{2\pi^2 \hbar^3 c^3} k_B^3 T_\gamma^3 \int \frac{\beta^3 E^2 dE}{e^{\beta E} - 1} = \frac{g}{2\pi^2 \hbar^3 c^3} k_B^3 T_\gamma^3 2.404, \quad (\text{B.5})$$

$$u_\gamma(T_\gamma) = \frac{g}{2\pi^2 \hbar^3 c^3} k_B^4 T_\gamma^4 \int \frac{\beta^4 E^3 dE}{e^{\beta E} - 1} = \frac{g}{2\pi^2 \hbar^3} k_B^4 T_\gamma^4 \frac{\pi^4}{15}. \quad (\text{B.6})$$

We note from Eq. (B.4) that we can define the energy density function for photons

$$\mathcal{U}(E) = \frac{du_\gamma}{dE} = \frac{g}{2\pi^2 \hbar^3 c^3} \frac{E^3}{e^{\beta E} - 1}, \quad (\text{B.7})$$

which states that the radiation of the early Universe has a black-body spectrum. As the Universe expanded and cooled, this radiation can still be detected and is now observed as the Cosmic Microwave Background (CMB) radiation. The current spectrum corresponds to a temperature of 2.725 K (Planck Collaboration et al. 2020). Integration of Eq. (B.3) for  $T_\gamma = 2.725$  K gives  $n_\gamma = 4.09649 \times 10^8$  photons  $\cdot m^{-3}$ .

### B.2. Baryon densities

**Neutrons and protons** To determine the total rate of  ${}^7\text{Be}$ -involving electroweak and strong nuclear reactions, it is necessary to compute the population factors for electrons, baryons, and neutrinos after NSE freeze-out in the 10–100 keV temperature range.

In this context, at  $t \sim 10^{-4}$  s after the Big Bang (or  $k_B T \sim$

100 MeV, where  $k_B$  is the Boltzmann constant), as the temperature fell below the rest masses of the heavier baryons, their abundances became exponentially suppressed and they efficiently annihilated with their antiparticles. Thus, at NSE freeze-out, only protons, neutrons, and their respective antiparticles essentially remained (Weinberg 2008a; Mukhanov 2005). Taking into account the large matter–antimatter asymmetry, the net baryon density is

$$n_b = n_{\hat{b}} - n_{\bar{b}} = n_p + n_n, \quad (\text{B.8})$$

with  $n_{\hat{b}} = n_{\hat{p}} + n_{\hat{n}}$ ,  $n_{\bar{b}} = n_{\bar{p}} + n_{\bar{n}}$  and we define the net proton and neutron densities as follows:

$$n_p = n_{\hat{p}} - n_{\bar{p}}, \quad n_n = n_{\hat{n}} - n_{\bar{n}}, \quad (\text{B.9})$$

where  $n_p$  and  $n_n$  are the proton and neutron number densities, while  $n_{\bar{p}}$  and  $n_{\bar{n}}$  are those of their respective antiparticles.

After decoupling from radiation down to weak freeze-out, weak processes determine the equilibrium abundance of different isospin states of nucleons through EC and AC on protons to form neutrons, free neutron decay to protons, and symmetric reactions involving their antiparticles. Denoting the neutron and proton masses by  $m_n$  and  $m_p$ , the  $Q$ -value of the reaction  $Q = (m_n - m_p)c^2 = 1.293$  MeV is comparable to the temperature at the NSE epoch ( $k_B T \approx 700$  keV). Boltzmann statistics then give

$$\frac{n_{\hat{n}}}{n_{\hat{p}}} = \frac{e^{-m_n c^2 / (k_B T)}}{e^{-m_p c^2 / (k_B T)}} = e^{-Q / (k_B T)}. \quad (\text{B.10})$$

At  $k_B T \approx 700$  keV, after the isospin flip ceases and only the excess baryons remain, protons and neutrons are classical, non-relativistic particles that obey Boltzmann statistics. Very few neutrons had undergone  $\beta^-$ -decay into protons (half-life  $\tau \approx 880.5$  s), as only  $t \lesssim 3.5$  seconds had elapsed since the Big Bang. The neutron ( $n_{\hat{n}}$ ) to proton ( $n_{\hat{p}}$ ) number density ratio at  $t \lesssim 3.5$  s can be determined as follows:

$$\frac{n_{\hat{n}}(t \approx 0)}{n_{\hat{p}}(t \approx 0)} = \frac{e^{-\frac{m_n c^2}{k_B T}}}{e^{-\frac{m_p c^2}{k_B T}}} = e^{-\frac{Q}{k_B T}} = 0.20. \quad (\text{B.11})$$

Between  $k_B T = 700$  keV and NSE freeze-out ( $k_B T = 100$  keV, approximately 300 s after the Big Bang), free neutrons can undergo  $\beta^-$ -decay into protons, following the exponential law  $n_{\hat{n}}(t) = n_{\hat{n}}(0)e^{-\frac{t}{\tau}}$ , where  $n_{\hat{n}}(0)$  is the initial number density of neutrons immediately after the Big Bang. On the other hand, the total number of nucleons  $n_{\text{tot}}$  is conserved:

$$n_{\text{tot}} = n_{\hat{p}}(0) + n_{\hat{n}}(0) = \frac{n_{\hat{n}}(0)}{0.20} + n_{\hat{n}}(0) = \frac{1.20}{0.20} n_{\hat{n}}(0) = 6n_{\hat{n}}(0), \quad (\text{B.12})$$

$$n_{\hat{p}}(t) = n_{\text{tot}} - n_{\hat{n}}(t) = 6n_{\hat{n}}(0) - n_{\hat{n}}(0)e^{-\frac{t}{\tau}}. \quad (\text{B.13})$$

Therefore after  $\approx 300$  s the ratio is (Perkins 2009)

$$\frac{n_{\hat{n}}(300 \text{ s})}{n_{\hat{p}}(300 \text{ s})} = \frac{n_{\hat{n}}(0)e^{-\frac{300}{\tau}}}{6n_{\hat{n}}(0) - n_{\hat{n}}(0)e^{-\frac{300}{\tau}}} \approx 0.135. \quad (\text{B.14})$$

At NSE,  $\beta^-$  decay almost completely stops because nearly all neutrons are bound in  $\alpha$  particles.

After weak freeze-out, the subsequent decrease in  $n_{\hat{n}}/n_{\hat{p}}$  is governed by free neutron  $\beta^-$  decay (half-life  $\tau \approx 880.5$  s), following the exponential law derived in Eq. (B.14):

$$\frac{n_{\hat{n}}(t)}{n_{\hat{p}}(t)} = \frac{e^{-t/\tau}}{6 - e^{-t/\tau}}, \quad (\text{B.15})$$

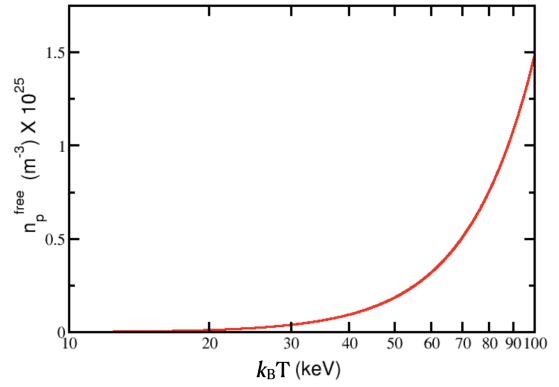


Fig. B.1: Free proton density ( $m^{-3} \times 10^{25}$ ) in total baryonic matter as a function of temperature  $k_B T$  (keV) for  $n_b = \eta \times n_\gamma$  ( $10 \text{ keV} < k_B T < 100 \text{ keV}$ ) baryons/m<sup>3</sup>, according to the Saha equation.

until NSE, after which almost all neutrons are bound in  $\alpha$  particles and can no longer decay, so the ratio  $n_{\hat{n}}/n_{\hat{p}}$  becomes fixed.

Using Eq. (B.15) from weak freeze-out down to NSE at  $T \lesssim 100$  keV, the neutron-to-proton abundance evolves over time due to isospin flip reactions and neutron  $\beta^-$  decay to

$$\frac{n_{\hat{n}}}{n_{\hat{p}}} = \frac{n_n}{n_p} \approx 0.135. \quad (\text{B.16})$$

Below the NSE epoch ( $100 \text{ keV} \gtrsim k_B T \gtrsim 10 \text{ keV}$ ), we can safely assume that all antibaryons have annihilated, while isospin flip reactions between  $^7\text{Li}$  and  $^7\text{Be}$  become significant. To determine the EC and PC rates, we must assess the fraction of free electrons and protons; that is, we need to subtract from their total density the number of protons and electrons bound in the nuclear species present at the NSE epoch. In this context, the Saha equation provides the equilibrium ratio between the product of the densities of free electrons and free protons (which are equal under the assumption of an electrically neutral Universe) and the total number of baryons (neutrons plus protons), including those in bound nuclear states, in a plasma. Therefore, it determines the density of protons relative to the total baryon density, and indirectly indicates how many protons are bound in nuclei and how many remain free. However, the abundance of light isotopes such as protium, deuterium, tritium, and  $^3\text{He}$  is negligible in NSE, with only  $^4\text{He}$  present (Fuller & Smith 2010). In fact, at NSE ( $k_B T \approx 0.1$  MeV), almost all protons are either free or bound in  $\alpha$  particles, while nearly all neutrons are bound in  $^4\text{He}$ .

In particular, applying the Saha equilibrium equation under NSE conditions shows that:

$$n_p(T) \approx \frac{15}{17} n_b(T) \approx \eta \frac{15}{17} n_\gamma(T), \quad (\text{B.17})$$

where the last relation follows from the WMAP-observed baryon-to-photon number density ratio  $\eta = n_b/n_\gamma = 6.11 \times 10^{-10}$  (Yu et al. 2022), assuming that  $\eta$  remains essentially constant after BBN. Using Eq. (B.16), the neutron density is

$$n_n(T) \approx 0.135 \times n_p(T) \approx \eta \frac{2}{17} n_\gamma(T). \quad (\text{B.18})$$

We note that the temperature dependence of the total photon density,  $n_\gamma(T) \propto T^3$  (see Eq. (B.5) in the Appendix B.1), can be derived by assuming a Bose-Einstein distribution for massless particles, which implies that the radiation in the early Universe had a black-body spectrum. Hence, from Eqs. (B.17) and (B.18),

Table B.1: Proton ( $n_p$ ), electron ( $n_{e^-}$ ), and positron ( $n_{e^+}$ ) number densities (in atomic units  $a_0^{-3}$ , where  $a_0$  is the Bohr radius), as well as the electron chemical potential relative to the electron mass ( $\mu_e - m_e c^2$ , with  $m_e c^2 = 18,775.13$  Hartrees), are given as functions of cosmic time since the Big Bang (first column, time in seconds) and the corresponding temperature in keV (second column). Note that  $n_p$  has been rescaled by  $10^7$ .

$t$ (s)	$k_B T$ (keV)	$n_p \times 10^7$ ( $10^{-7} a_0^{-3}$ )	$n_{e^-}$ ( $a_0^{-3}$ )	$n_{e^+}$ ( $a_0^{-3}$ )	$\mu_e - m_e c^2$ (a.u.)
3.156	87.233	16.8120	88.3470137	88.3470121	-18778.865
7.964	54.913	4.1938	1.26692624	1.26692582	-18778.865
20.098	34.568	1.0461	2.47121238e-03	2.47110776e-03	-18778.838
50.719	21.760	0.2609	2.10035855e-07	1.83939709e-07	-18725.819
127.990	13.698	0.0651	6.50968418e-09	9.70e-19	-13083.666
322.989	8.623	0.0162	1.62384586e-09	1.03e-37	-8491.340
815.074	5.428	0.0041	4.05069692e-10	6.44e-68	-5504.808
2,056.872	3.417	0.0010	1.01044983e-10	4.34e-116	-3546.005
5,190.598	2.151	0.0003	2.52057531e-11	1.35e-192	-2281.927
13,098.677	1.354	0.0001	6.28759452e-12	5.14e-314	-1472.696
31,560.000	0.872	0.00002	1.68120328e-12	$\approx 0.0$	-970.181

at the NSE epoch, out of 17 baryons, about 2 are neutrons and 15 are protons, either free or bound in nuclei. Moreover, assuming that light nuclei (D,  $^3\text{He}$ ,  $^3\text{H}$ , etc.) are negligible and only  $\alpha$  particles exist at the NSE epoch, among 17 baryons,  $2p + 2n$  are in  $^4\text{He}$ , while 13 are free protons. Finally, the free proton density is

$$n_p^{\text{free}}(T) \approx \frac{13}{17} n_b = \eta \frac{13}{17} n_\gamma(T). \quad (\text{B.19})$$

For  $10 \text{ keV} < k_B T < 100 \text{ keV}$ , we have  $1.4813 \times 10^{22} \text{ m}^{-3} < n_p^{\text{free}} < 1.4813 \times 10^{25} \text{ m}^{-3}$ , as shown in Fig. (B.1), where the fraction of free protons is plotted as a function of increasing temperature. In Tab. (B.1), the net number densities of protons at selected thermal energies relevant to the post-NSE epoch are provided.

### B.3. Lepton densities

**Electrons** Similarly, we define the net electron number density as

$$n_e = n_{e^-} - n_{e^+}, \quad (\text{B.20})$$

where  $n_{e^-}$  and  $n_{e^+}$  are the electron and positron number densities, respectively. Assuming the large-scale charge neutrality of the Universe (Caprini & Ferreira 2005; Cameron 2022) implies that

$$n_e = n_p. \quad (\text{B.21})$$

Thus, once the net proton density  $n_p$  is known at a given epoch (see Eq. (B.17)), the net electron density is also determined and can be used to compute the EC rate at that time.

**Neutrinos** Another process that may contribute to the destruction of  $^7\text{Be}$  is AC, Eq. (3). The relevant question is whether a significant population of antineutrinos is present during the NSE epoch. After weak decoupling, neutrino–antineutrino pairs cease to interact with the ( $e^- e^+$ ) plasma and subsequently free-stream, analogous to CMB photons after photon decoupling. Like the CMB, relic neutrinos retain a thermal distribution, but unlike photons, they obey Fermi–Dirac statistics:

$$dn_\nu(E) = \frac{g}{2\pi^2 \hbar^3 c^3} k_B^3 T_\nu^3 \frac{\beta^3 E^2 dE}{e^{\beta E} + 1}, \quad (\text{B.22})$$

where  $\beta = kT_\nu$ . The energy dispersion is given by  $E = pc$  due to the small mass of the neutrino. Note that for neutrinos,  $g = 1$  since they interact via the weak interaction, which only couples to left-handed neutrinos. The total density of neutrinos is

$$n_\nu(E) = \frac{g}{2\pi^2 \hbar^3 c^3} k_B^3 T_\nu^3 \int \frac{\beta^3 E^2 dE}{e^{\beta E} + 1} = \frac{g}{2\pi^2 \hbar^3 c^3} k_B^3 T_\nu^3 \frac{3}{4} 2.404. \quad (\text{B.23})$$

In Eq. (B.23),  $T_\nu$  differs from the photon temperature  $T_\gamma$ , as neutrinos decouple from photons once they decouple from electrons and are therefore no longer in thermal equilibrium.

The relic neutrino number density is obtained from Eq. (B.23) and may be compared directly with the photon number density in Eq. (B.5) to give:

$$n_\nu = \frac{3}{4} \frac{g_\nu}{g_\gamma} \left( \frac{T_\nu}{T_\gamma} \right)^3 n_\gamma, \quad (\text{B.24})$$

where  $g_\nu = 2$  and  $g_\gamma = 1$  for a single helicity state (electron neutrinos and antineutrinos each carry one helicity state, thus we use  $g_\nu = 2$  for the combined  $\nu_e - \bar{\nu}_e$  population). Moreover, after  $e^- e^+$  annihilation, photon and neutrino temperatures are related by (Dolgov 2002; Weinberg 2008b)

$$T_\nu = \left( \frac{4}{11} \right)^{1/3} T_\gamma, \quad (\text{B.25})$$

which, using Eq. (B.24), yields

$$n_\nu = \frac{g_\nu}{g_\gamma} \frac{3}{11} n_\gamma, \quad (\text{B.26})$$

for each of the neutrino flavours, including muon ( $\nu_\mu$ ) and tau ( $\nu_\tau$ ) neutrinos. Electron neutrino–antineutrino densities are reported in Tab. (B.2). These values may be multiplied by three to include the  $\nu_\mu - \bar{\nu}_\mu$  and  $\nu_\tau - \bar{\nu}_\tau$  contributions because, before their annihilation,  $\mu^\pm$  and  $\tau^\pm$  pairs were also in thermal equilibrium with the radiation field. Both  $\nu_\mu$  and  $\nu_\tau$  decouple from the primordial plasma while their associated charged leptons are still present in significant abundance. Consequently, they undergo thermal freeze-out with a number density comparable to that of electron neutrinos. Subsequently, the muons and tauons decay into their respective associated neutrinos.

$k_B T$ (keV)	$n_\gamma$ (m $^{-3}$ )	$n_{\nu+\bar{\nu}}$ (m $^{-3}$ )
10	$3.17027 \times 10^{31}$	$8.64618 \times 10^{30}$
20	$2.53621 \times 10^{32}$	$6.91695 \times 10^{31}$
30	$8.55972 \times 10^{32}$	$2.33447 \times 10^{32}$
40	$2.02897 \times 10^{33}$	$5.53356 \times 10^{32}$
50	$3.96283 \times 10^{33}$	$1.08077 \times 10^{33}$
60	$6.84778 \times 10^{33}$	$1.86758 \times 10^{33}$
70	$1.08740 \times 10^{34}$	$2.96564 \times 10^{33}$
80	$1.62318 \times 10^{34}$	$4.42685 \times 10^{33}$
90	$2.31112 \times 10^{34}$	$6.30307 \times 10^{33}$
100	$3.17027 \times 10^{34}$	$8.64618 \times 10^{33}$

Table B.2: Density of neutrino+antineutrino pairs  $n_\nu + n_{\bar{\nu}}$  at the epoch of NSE calculated from the photon number density  $n_\gamma$  (see Eq. (B.26) in the main text). To obtain the number density of neutrinos (or antineutrinos) only, divide the third column by 2, as we set  $\mu_\nu = 0$ .

#### B.4. Proton and electron chemical potentials

Once  $n_p(T) = n_e(T)$  is known, we can determine the chemical potentials of these species at NSE, assuming that a system of  $e^-$  and  $e^+$  pairs can be modelled as a Fermi gas in thermal equilibrium with the  $\gamma$  radiation, thus characterised by their temperature and a single chemical potential via a relativistic energy-momentum dispersion relation. While in the upper part of our temperature range ( $k_B T \geq 50$  keV), electrons and positrons remain in pair equilibrium ( $\mu_\gamma = 0$ ,  $\mu_{e^+} = -\mu_{e^-} \equiv -\mu_e$ ), at lower temperatures positrons progressively freeze out and annihilate. In particular, the assumption of pair equilibrium breaks down below  $k_B T \approx 20$  keV ( $\mu_\gamma \neq 0$ ). In this temperature regime, in principle  $\mu_{e^+} \neq -\mu_{e^-}$ , and one should determine the chemical potentials of particles and their respective antiparticles using kinetic equations. This task is well beyond the scope of this contribution; therefore, we assume that the Fermi gas is in equilibrium and that a single chemical potential describes both species.

In this context, matter-antimatter asymmetry can be described as a non-zero chemical potential for particle extraction from, or insertion into, the Fermi sea. Consider a gas of positron-electron pairs. Decoupling of electrons occurs at  $k_B T \approx 1$  MeV ( $t \approx 1.71$  s), after the weak decoupling of neutrinos. At this epoch, electrons are relativistic, and their number density is given by

$$n_{\hat{e}}(T) = \frac{g_i}{2\pi^2 \hbar^3 c^3} \int \frac{\sqrt{E^2 - m_e^2 c^4} E \, dE}{\exp[\beta(E - \mu_e)] + 1}, \quad (\text{B.27})$$

where  $E$  is the relativistic kinetic energy,  $\mu_e$  is the electron (or positron) chemical potential, and  $m_e$  is the electron mass.

Similarly, the antiparticle number density is

$$n_{\hat{e}}(T) = \frac{g_i}{2\pi^2 \hbar^3 c^3} \int \frac{\sqrt{E^2 - m_e^2 c^4} E \, dE}{\exp[\beta(E + \mu_e)] + 1}. \quad (\text{B.28})$$

Owing to the particle-antiparticle asymmetry, the electron net number density is the difference between Eqs. (B.27) and (B.28)

$$\begin{aligned} n_e(T) &= \frac{g_e}{2\pi^2 \hbar^3 c^3} \int \frac{\sqrt{E^2 - m_e^2 c^4} E \, dE}{e^{\frac{E-\mu_e}{k_B T}} + 1} \\ &- \frac{g_e}{2\pi^2 \hbar^3 c^3} \int \frac{\sqrt{E^2 - m_e^2 c^4} E \, dE}{e^{\frac{E+\mu_e}{k_B T}} + 1} = n_p(T), \end{aligned} \quad (\text{B.29})$$

where the last equality implies charge neutrality, as in Eq. (B.21). In Eq. (B.29), while electrons become mildly relativistic in the

range  $10$  keV  $< k_B T < 100$  keV and therefore the relativistic particle dispersion law is used, protons remain deeply non-relativistic over the entire temperature range considered here. In Tab. (B.1), the number densities of electrons and positrons at selected thermal energies relevant to the post-NSE epoch are reported. Given  $n_p(T)$  from Eq. (B.17), we can, in principle, obtain  $\mu_e(T)$  by inverting Eq. (B.29). Once  $\mu_e$  is known, the densities of electrons and positrons, as well as their population factors entering the EC rate, can be obtained directly from the respective Fermi-Dirac distributions in Eq. (B.29) for particles and antiparticles. Although the electron number density reaches values well above solid density (approximately three orders of magnitude higher; see the fourth column in Tab. (B.1)), the high temperatures considered here keep the leptonic component in the non-degenerate regime. However, degeneracy increases as temperature decreases ( $0.006 < n_e \lambda_T^3 < 0.2$ , where  $\lambda_T \propto T^{-1/2}$  is the thermal de Broglie wavelength).

In the last column of Tab. (B.1), we present the electron chemical potential over the temperature range in which isospin flip drives the  $^7\text{Li}-^7\text{Be}$  equilibrium via Eq. (2), using a bisection method to invert Eq. (B.29). As the temperature decreases, the electron chemical potential  $\mu_e$  increases (becomes less negative; see the last column of Tab. (B.1); please note that  $\mu_e$  is defined relative to the electron rest mass  $m_e c^2 = 18,775.13$  Hartrees), reflecting the gradual increase in the degeneracy parameter throughout the evolution. Moreover, the positron and electron number densities (see Tab. (B.1)) are nearly identical at high temperatures ( $k_B T \geq 50$  keV), implying that the net electron number density  $n_e$  is almost zero. In contrast, in the low-temperature regime (below 20 keV), a non-zero  $\mu_e$  (see Tab. (B.1)) produces the required particle-antiparticle imbalance imposed by global charge neutrality. Therefore, at the higher end of our temperature range, electrons and positrons remain almost in pair equilibrium, while at lower temperatures, positrons progressively freeze out and annihilate, disrupting pair equilibrium.

Similarly, one can obtain the chemical potential of protons at NSE from Eq. (B.29), even though we do not treat them as relativistic particles in our calculations.

#### B.5. Neutrino chemical potential

In contrast to electrons and positrons, we assume a vanishing neutrino chemical potential,  $\mu_\nu = 0$ . Before weak freeze-out, neutrinos remain in thermal equilibrium with photons and  $e^-e^+$  pairs through

$$\gamma + \gamma \longleftrightarrow e^- + e^+ \longleftrightarrow \nu_e + \bar{\nu}_e. \quad (\text{B.30})$$

This assumption is justified by the very small lepton-antilepton asymmetry at weak freeze-out ( $k_B T \simeq 3$  MeV,  $t \simeq 0.2$  s). In particular, the difference between the electron and positron number densities is negligible:

$$(n_{\hat{e}^-} - n_{\hat{e}^+})|_{kT=3 \text{ MeV}} \approx 0. \quad (\text{B.31})$$

Since electrons and positrons have equal abundances at that stage, neutrinos and antineutrinos also freeze out with equal number densities, which implies  $\mu_{\nu_e} \approx 0$  for all neutrino flavours.

## Appendix C: $^7\text{Be}$ to $^7\text{Li}$ Decay rates

Table C.1: Excited to excited decay rates as a function of temperature (keV) or time since the Big Bang (s).  $R_{e^-}$ : electron capture;  $R_{e^+}$ : positron decay;  $R_{\bar{\nu}}$ : antineutrino capture.

$t$ (s)	$k_B T$ (keV)	$R_{e^-}$ (s $^{-1}$ )	$R_{e^+}$ (s $^{-1}$ )	$R_{\bar{\nu}}$ (s $^{-1}$ )
3.156	87.23	3.693e-08	3.089e-06	3.053e-06
7.964	54.91	3.445e-08	1.831e-06	1.797e-06
20.10	34.57	1.046e-07	2.471e-03	2.471e-03
50.72	21.76	2.610e-08	2.100e-07	1.839e-07
127.99	13.70	6.510e-09	6.510e-09	9.698e-19
322.99	8.623	1.624e-09	1.624e-09	1.029e-37
815.07	5.428	4.051e-10	4.051e-10	6.435e-68
5190.6	2.151	2.521e-11	2.521e-11	1.349e-192
13099	1.354	6.288e-12	6.288e-12	5.143e-314
31560	0.8723	1.681e-12	1.681e-12	0.0

Table C.4: Ground to excited decay rates as a function of temperature (keV) or time since the Big Bang (sec).  $R_{e^-}$ : electron capture;  $R_{e^+}$ : positron decay;  $R_{\bar{\nu}}$ : antineutrino capture.

$t$ (s)	$k_B T$ (keV)	$R_{e^-}$ (s $^{-1}$ )	$R_{e^+}$ (s $^{-1}$ )	$R_{\bar{\nu}}$ (s $^{-1}$ )
3.156	87.23	6.444e-08	0.0000	4.523e-10
7.964	54.91	1.277e-09	0.0000	2.035e-12
20.10	34.57	2.471e-12	0.0000	1.027e-15
50.72	21.76	2.100e-16	0.0000	9.104e-20
127.99	13.70	6.510e-18	0.0000	3.622e-21
322.99	8.623	1.624e-18	0.0000	8.789e-22
815.07	5.428	4.051e-19	0.0000	2.239e-22
5190.6	2.151	2.521e-20	0.0000	2.315e-23
13099	1.354	6.288e-21	0.0000	7.445e-24
31560	0.8723	1.681e-21	0.0000	2.815e-24

Table C.2: Excited to ground decay rates as a function of temperature (keV) or time since the Big Bang (sec).  $R_{e^-}$ : electron capture;  $R_{e^+}$ : positron decay;  $R_{\bar{\nu}}$ : antineutrino capture.

$t$ (s)	$k_B T$ (keV)	$R_{e^-}$ (s $^{-1}$ )	$R_{e^+}$ (s $^{-1}$ )	$R_{\bar{\nu}}$ (s $^{-1}$ )
3.156	87.23	3.862e-07	2.449e-06	1.016e-06
7.964	54.91	5.259e-09	2.579e-06	2.078e-07
20.10	34.57	1.027e-11	2.630e-06	4.529e-08
50.72	21.76	9.104e-16	2.630e-06	1.027e-08
127.99	13.70	3.622e-17	2.630e-06	2.422e-09
322.99	8.623	8.789e-18	2.630e-06	5.807e-10
815.07	5.428	2.239e-18	2.630e-06	1.407e-10
5190.6	2.151	2.315e-19	2.630e-06	8.572e-12
13099	1.354	7.445e-20	2.630e-06	2.118e-12
31560	0.8723	2.815e-20	2.630e-06	5.665e-13

Table C.3: Ground to ground decay rates as a function of temperature (keV) or time since the Big Bang (sec).  $R_{e^-}$ : electron capture;  $R_{e^+}$ : positron decay;  $R_{\bar{\nu}}$ : antineutrino capture.

$t$ (s)	$k_B T$ (keV)	$R_{e^-}$ (s $^{-1}$ )	$R_{e^+}$ (s $^{-1}$ )	$R_{\bar{\nu}}$ (s $^{-1}$ )
3.156	87.23	5.233e-07	0.0000	3.628e-07
7.964	54.91	7.332e-09	0.0000	2.814e-09
20.10	34.57	4.533e-11	0.0000	1.027e-11
50.72	21.76	1.030e-14	0.0000	9.104e-16
127.99	13.70	2.422e-15	0.0000	3.622e-17
322.99	8.623	5.807e-16	0.0000	8.789e-18
815.07	5.428	1.407e-16	0.0000	2.239e-18
5190.6	2.151	8.572e-18	0.0000	2.315e-19
13099	1.354	2.118e-18	0.0000	7.445e-20
31560	0.8723	5.665e-19	0.0000	2.815e-20